Aeroelastic analysis using confocal sensors: experimental study and numerical validation with application to a future particle detector

Aitor Amatriain*[a,b], Massimo Angeletti[a], Corrado Gargiulo[a], Gonzalo Rubio[b,c]

[a] *ALICE Collaboration, CERN, Geneva 23, 1211, Switzerland*
[b] *E.T.S. Ingeniería Aeronáutica y del Espacio, Universidad Politécnica de Madrid, Plaza Cardenal Cisneros 3, 28040, Madrid, Spain*
[c] *Center for Computational Simulation, Universidad Politécnica de Madrid, Campus de Montegancedo, Boadilla del Monte, 28660, Madrid, Spain*

Abstract

This study investigates the structural displacements induced by aerodynamic loads in a future particle detector at the Large Hadron Collider (LHC): the Inner Tracking System 3 (ITS3) of the ALICE experiment. The development of an ultralight structure and the air cooling lead to an unprecedentedly low material budget, resulting in improved accuracy compared to the current detector (ITS2). The airflow applied to the low-mass structure of the ITS3 is expected to cause vibrations, which requires an aeroelastic analysis that is performed using experimental and numerical methods. A novel experimental approach is proposed using confocal chromatic sensors to measure the structural displacements of an ITS3 prototype with submicron accuracy. A simplified mathematical model is developed for the fluid-structure interaction. The results obtained in the experimental setup show that the numerical model predicts the primary peaks in the spectrum of structural displacements induced by airflow. The validated model is used to analyze both the real anticipated configuration of the future ITS3 setup and potential modifications arising from changes in detector cooling and installation requirements.

Keywords:
Large Hadron Collider, ALICE experiment, Air cooling, Fluid-structure interaction

1. Introduction

Vibration control is a key in industrial applications to avoid failure of mechanical components. Relevant sources of vibration include pressure fluctuations coming from the environment [1], mass imbalances [2], irregular mechanical contacts [3], and moving parts [4]. Different solutions are frequently explored, namely the improvement of structural stiffness [5], or the addition of vibration absorbers that increase the damping of systems [6]. These solutions have limitations when applied to a wide range of frequencies and external loads, which motivate the development of variable stiffness devices [7, 8]. A complex discipline in the study of vibrations is

aeroelasticity, which consists of the coupling between aerodynamic loads and structural dynamics. Aeroelastic problems are present in multiple engineering applications, namely aircraft wings [9], turbomachinery [10], and civil structures [11]. The prediction of the structural response is required in these applications, as positive feedback between structure motion and external forces can cause problems due to fatigue or large displacements [12]. For example, aeroelasticity is an important part of aircraft design, given that aeroelastic instabilities such as divergence [13], flutter [14], and buffet [15] can lead to structural failure at different levels of importance.

The Large Hadron Collider (LHC) is the world's largest and highest-energy particle collider, and vibration studies are required in multiple parts of the infrastructure. The magnetic fields generated by magnets are measured using a rotating coil system that induces vibrations [16]. Future measurement needs will require an increase in the speed of the rotating components, which will imply an increase in vibration amplitudes [17]. The installation of new equipment during the LHC operation may affect the quality of the measurements for similar reasons [18]. Other sources of noise during LHC operation are earth movements and humans, both commonly referred to as cultural noise [19]. Since not all components of large experiments are built at CERN, vibrations due to transport loads are also an important concern [20, 21].

ALICE (A Large Ion Collider Experiment) is one of the four large experiments at the LHC. The Inner Tracking System (ITS) is the closest detector to the beam pipe, where particle collisions are produced. During the Long Shutdown 3 (2026-2030), the innermost part (Inner Barrel, IB) of the current system (Inner Tracking System 2, ITS2) will be replaced by the Inner Tracking System 3 (ITS3). The ITS3 IB will consist of two halves, named half-barrels, to allow the detector to be mounted around the beam pipe (see Fig. 1a). Each half-barrel will incorporate three layers made of a single large silicon pixel chip of length 280 mm, thickness of 40 µm, and radii 18-24-30 mm, which will be bent in a half-cylindrical shape (see Fig. 1b).

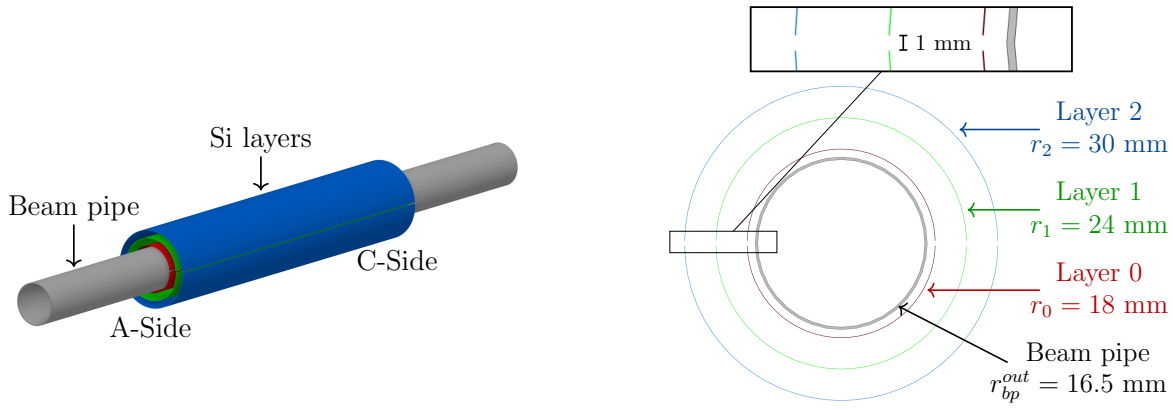

(a) Isometric view.

(b) Front view.

Fig. 1: Inner barrel of the ALICE ITS3.

The ALICE ITS3 will be the first particle detector at CERN to use a cooling system based

on forced air convection. The heat dissipation of the silicon sensors will be non-uniform, with the highest heat dissipation near the A-Side (see Fig. 2a). The proposed design considers the use of thermally-conductive open-cell carbon foam rings (K9 foam) in that zone, in contact with the silicon sensors. These foams act as heat exchangers, so heat is transferred from the sensors to the foams by conduction, and then it is removed from the foams by convection to the air. The A-Side rings are insufficient to keep the silicon sensors in cylindrical shape, and the design includes additional foam parts made of lighter and less conductive foam (RVC foam) as mechanical supports. Due to the complexity of the installation of the ITS3 in the ALICE cavern, the system is not expected to be completely isolated; therefore, pressure drop should be minimized to reduce the leak rate. To this end, holes are drilled into the foams. This design will result in a material budget value per layer equal to $X/X_0 \approx 0.06\%$, which is the lowest value ever achieved in a HEP particle detector, with a reduction of 80% with respect to the ITS2 ($X/X_0 \approx 0.28\%$). Minimizing the value of the material budget is crucial, since the overall performance of a particle detector improves because the uncertainty of the measurements of particle momenta is reduced [22]. Additional details about the foam characterization are available in [23], while the cooling system design process and thermal analysis can be found in [24]. The cooling system of the ALICE ITS3 must ensure that not only the silicon layers do not break, but that the displacements are lower than the accuracy of the silicon sensors, which is between 4 and 6 µm. Thus, an aeroelastic study is needed to predict the effects of the airflow on the mechanical behavior of the silicon layers, which requires the development of a mathematical model and an experimental prototype. Following a conservative approach, the target of the maximum displacement to the equilibrium position is set to 1 µm.

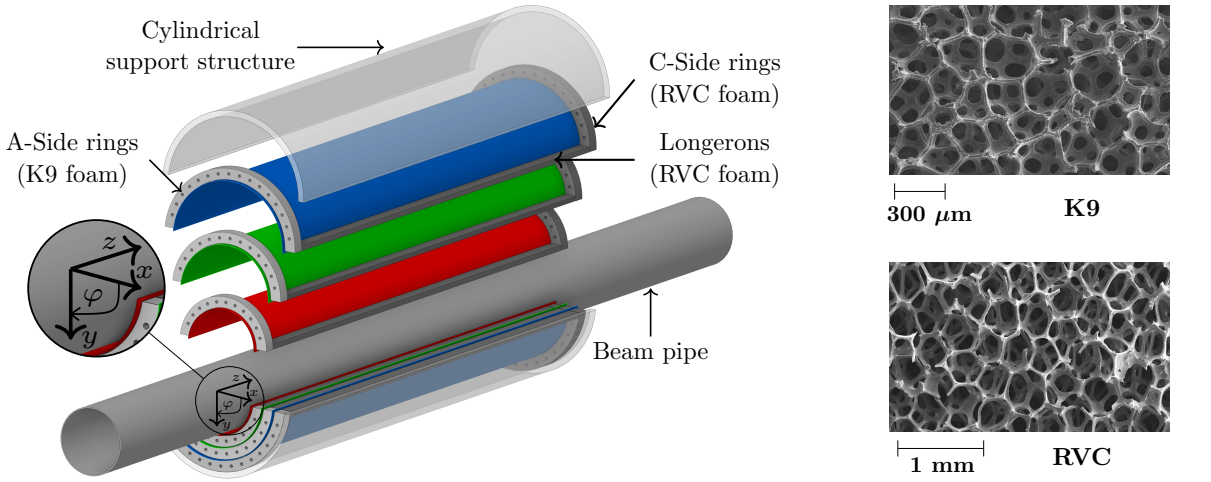

(a) Isometric view.

(b) Microscope images of foams.

Fig. 2: Foam structures of the inner barrel of the ALICE ITS3.

Numerical simulations of the Fluid-Structure Interaction (FSI) require model selection for

fluid and structural equations, as well as the definition of the coupling strategy. The universal approach to solving the structural problem consists of considering a spring-damper-mass system of equations, and the coefficients are built based on material stiffness, mass, and damping properties [25, 26]. Simplified geometries and methods for structural analysis allow the reduction of the computational cost, in particular in complex materials such as composites [27, 28, 29, 30]. The complexity of the fluid problem is higher, due to the disparity between the small and large scales of fluid flows. In computational fluid dynamics, different equations are solved depending on mesh and accuracy requirements. Direct Numerical Simulations (DNS) directly solve the Navier Stokes equations, which results in the lowest modeling error [31]. However, for moderate to high Reynolds numbers, the computational cost associated with these simulations is beyond the capabilities of current computing power within the industrial framework. Large Eddy Simulations (LES) reduce the computational cost by approximately one order of magnitude, which is still limiting for industrial cases, although recent investigations show promising results using the latest advances in numerical methods [32]. In Reynolds-Averaged-Navier Stokes (RANS) models, the computational cost is several orders of magnitude lower than in LES, and it does not depend on the Reynolds number. RANS models are interesting alternatives in highly unstable flows or when the mean flow quantities are responsible for structural deformations. However, the required meshes are still too fine for practical applications, and large errors have been found for non-optimal meshes [33]. Hybrid RANS/LES models take the advantages of RANS and LES and provide the optimum balance between computational cost and accuracy [34], although current studies at high Reynolds numbers are limited to coarse meshes [35]. Thus, baseline tools in the aeronautical industry, where aeroelastic studies are common, comprise only structural simulations with aerodynamic forces computed from simplified models such as the Blade Element Momentum Theory (BEMT, [36]), Free Vortex Methods (FVM, [37]), and Theodorsen functions [38].

In fluid simulations, equations are usually solved in Eulerian coordinates, while a Lagrangian description is the standard approach for structural simulations. This leads to numerical challenges to solve the resulting system of equations, in which the coupling between the equations of fluid and structural problems plays an important role. The most popular coupling techniques are monolithic and partitioned. In the monolithic case, fluid and structural domains are treated as a single continuum, and all equations are solved simultaneously [39, 40]. In partitioned solvers, the fluid and structural equations are solved separately, and the coupling is achieved through an iterative procedure [41, 42]. Monolithic methods are more stable, although at the cost of increased complexity in implementation and computational cost [43]. In monolithic methods, different solutions exist to deal with the difference on the formulations of fluid and structural equations, ranging from fully Eulerian [44] to fully Lagrangian [45]. Arbitrary Lagrangian-Eulerian (ALE) methods are intermediate options in which structural equations are solved in

Lagrangian coordinates, and fluid equations are solved in an artificial coordinate system [46]. Computational cost savings can also be obtained with the Immersed Boundary Methods (IBM), although their applicability for flows at high Reynolds numbers is limited due to their diffuse nature [47]. The accuracy and stability of the simulations are strongly influenced by the quality of the dynamic meshing approach used, especially when large displacements are considered [48, 49]. Even if there are some cases in which the computational cost of FSI simulations is affordable using reduced-size meshes, such as in medical applications [50, 51], the high computational cost of FSI problems usually motivates the decoupling of structural and fluid simulations in the partitioned approach. Loosely-coupled (or explicit) FSI simulations, in which only one iteration is performed at every time step, are an alternative to coupled FSI that provide successful results in particular cases without important nonlinearities [52, 53]. Structural and fluid problems are solved separately in decoupled approaches, which provide a reasonable result for preliminary studies and/or when structural displacements are small [54, 55]. Given the computing power limitations in the industry and the complexity of FSI simulations, experimental works are also extensive in aeroelasticity, especially in the study of wings [56, 57, 58, 59].

In the ALICE ITS3, the Reynolds number of the airflow (based on the channel height $h = 6$ mm) to meet the thermal requirements is $Re_h \approx 3000$. Assuming that circular pipe flow regimes are applicable, the fully developed channel flow is transitional, while the holes of the foams generate a turbulent free shear flow [24]. To study the vibrations generated by the airflow, the application of simplified models such as those mentioned in the previous paragraph is discarded, since they have been developed for wing profiles. On the other hand, RANS turbulence models are unsuitable for free shear turbulent flows. Thus, more computationally-demanding simulations are required, such as LES, which is the choice for the current work. This implies the definition of fine meshes, which means that, in the industrial framework, a simplified and specially tailored model needs to be developed by taking into account the fundamental physics of the problem. Furthermore, the experimental validation of displacements of ALICE ITS3 layers is a challenge, as the tight tolerances and low system mass do not allow using invasive devices such as accelerometers [60]. The standard non-invasive techniques used in engineering, namely laser triangulation sensors, have been verified by the authors as unsuitable due to the tight tolerances of the system. Thus, more accurate devices are needed for this particular case. In the current study, the use of confocal chromatic sensors for displacement is proposed. On the basis of thorough market research by the authors, they provide up to one order of magnitude greater accuracy than laser displacement sensors. To the authors' knowledge, this is the first publication on the use of confocal sensors in a high-level engineering application.

The paper is structured as follows: in Section 2.1, the experimental setup employing confocal sensors to measure the displacements of the layers in a prototype of the ALICE ITS3 is presented. Next, in Section 2.2 a mathematical model for the fluid-structure interaction (FSI)

is developed; in particular, it focuses on decoupling the fluid and structural problems, and the novel methodology followed in the fluid simulations is applicable to other aeroelastic problems that combine different flow physics. The results of the study are detailed in Section 3. Initially, the mathematical model is compared with experimental values for validation. Subsequently, the model is used to analyze the real configuration of the future ITS3 setup, as well as potential modifications due to changes in detector cooling and installation requirements. Finally, in Section 4 the most significant findings are summarized.

2. Methodology

The aeroelastic study of the ALICE ITS3 is divided into two parts. First, in Section 2.1 an experimental setup based on the design outlined in Fig. 2a and installed in a wind tunnel is presented. Confocal sensors are installed in this setup to measure the displacements of the layers in a prototype of the ALICE ITS3. Second, Section 2.2 describes the development of a mathematical model for the fluid-structure interaction (FSI). This model aims to determine the aeroelastic performance of the system by decoupling the fluid and structural problems and employing simplified geometry in the fluid simulations.

2.1. Experimental setup

The experimental setup presented first in [24] for thermal analysis is used to measure the displacements of Layer 2 (see Fig. 1b). Layer 2 exhibits the highest displacements in the setup, a point that will be justified later. Figure 3a shows the core of the setup, which consists of a prototype of a half-barrel of the design of Fig. 2a and a carbon sandwich cover including a Carbon-Fiber Reinforced Plastic (CFRP+thermally-insulating foam+CFRP). The cover has an inner radius of 40 mm, instead of the 36 mm required (30 mm of the radius of Layer 2 shown in Fig. 1b + 6 mm of the foam). This is because it was previously manufactured for a preliminary 40 mm of inner radius model; it was decided to adapt it to the current design. To solve the mismatch in the dimensions, a thermally-insulating closed-cell carbon foam is introduced to cover the remaining 4 mm of thickness (see Fig. 3c). Holes of 1.5 mm of diameter are drilled in the longerons so that the wires of the temperature sensors can exit the system (see Fig. 3c).

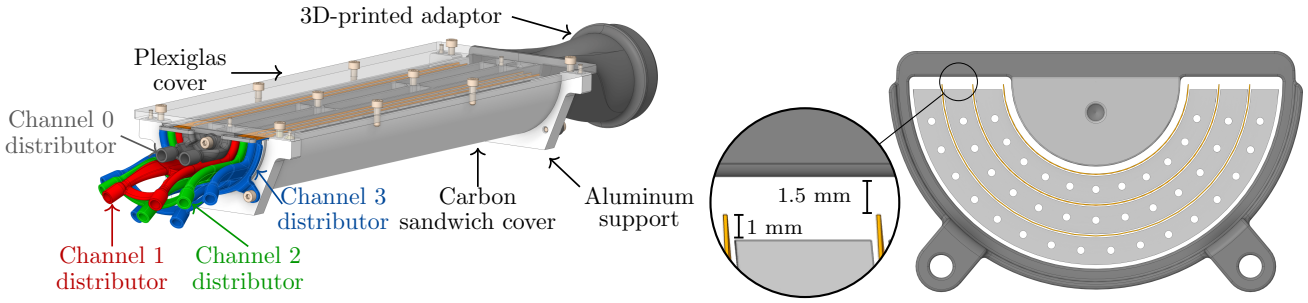

(a) Isometric view.

(b) Front view (C-Side).

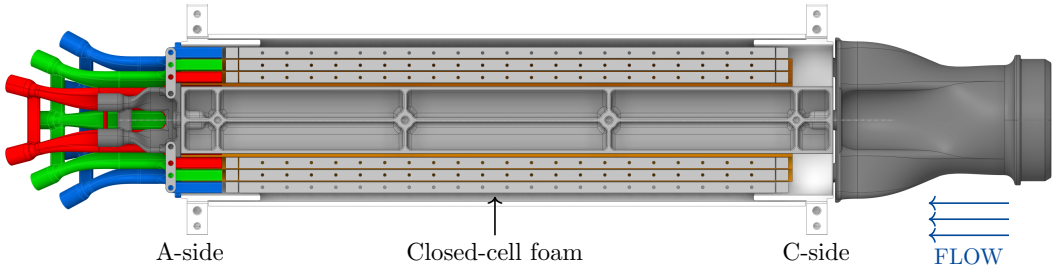

(c) Top view.

Fig. 3: ALICE ITS3 half-barrel used in the experimental setup.

The flow distribution system consists of four separated channels (see Fig. 3a). At the C-side, the transition from a circular pipe of 25 mm of radius to the prototype of 16.5 mm of inner radius and 36 mm of outer radius is done with a 3D-printed adaptor. The detailed adaptor geometry is irrelevant for the current work [24]. The layers used in this setup consist of the following materials: polyimide (12.5 µm) - silicon (40 µm) - polyimide (12.5 µm) - copper (5 µm) - polyimide (12.5 µm). These layers are glued with epoxy glue for a total thickness of approximately 165 µm, which means that the total thickness of the glue is 165 - 3×12.5 - 40 = 87.5 µm. Since there are four glue layers, assuming that the glue quantity is equally distributed in all layers, the thickness of each glue layer is 87.5 µm/4 $\approx$ 22 µm.

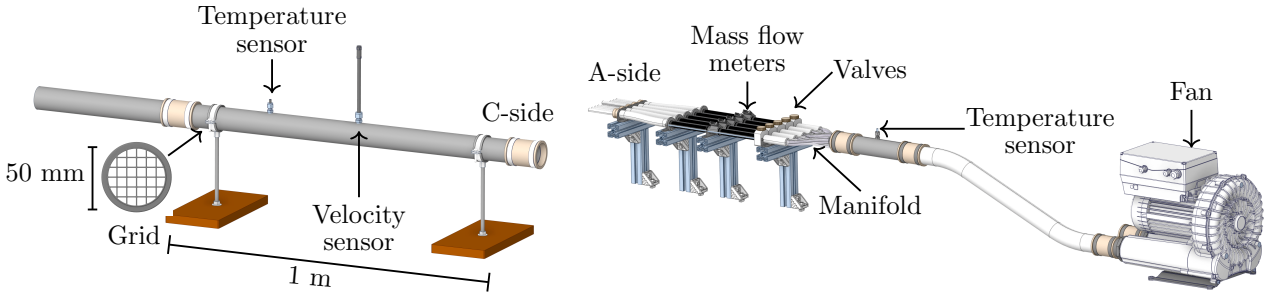

(a) Inlet. (b) Outlet.

Fig. 4: Components of the wind tunnel.

The airflow is generated by a fan that can provide up to 2×10^4 Pa for a freestream velocity of 20 m/s and includes a frequency inverter so that the operating point can be set manually or with a computer. The flow direction is from the C-side to the A-side (see Fig. 3c). All channels are equipped with an aluminum valve and a mass flow meter that have an uncertainty of $\pm 0.07 v_\infty$ (see Fig. 4b). Channel 3 uses two mass flow meters due to limitations in the range of the devices. The mean freestream velocity in the four half-barrels $v_{\infty,i}$ (i from 1 to 4) is obtained by mass conservation, assuming that the flow is steady and incompressible. The valves have been designed and produced at CERN to minimize the pressure loss in that area.

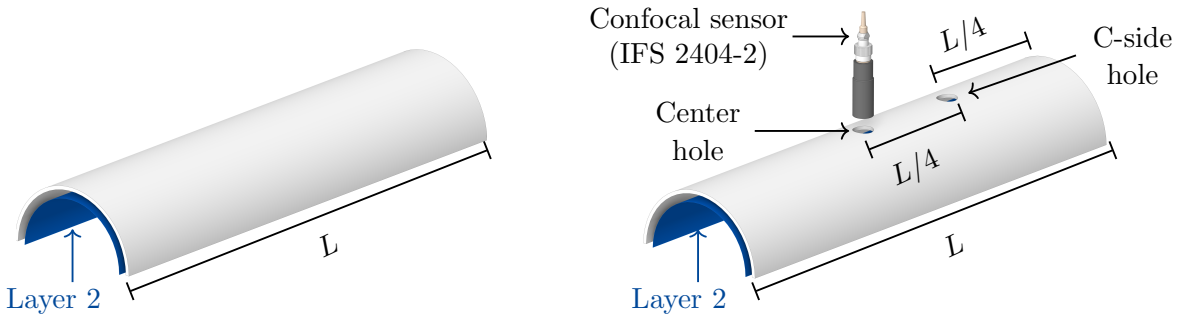

(a) Old. (b) New.

Fig. 5: Update of the prototype of Fig. 3 to measure Layer 2 displacements

In this work, a modification is carried out to the prototype of Fig. 3. Since the carbon sandwich cover is glued to the foams, it cannot be replaced by a new one; thus, two holes of 12 mm of diameter are drilled at $x = 0$ (see Fig. 5). These holes are subsequently covered by a transparent glass, so that the displacements of Layer 2 can be measured with a confocal chromatic sensor.

2.1.1. Confocal chromatic sensors

Confocal chromatic sensors use white light to measure distances and thicknesses of materials. These sensors contain a multilens optical system that disperses the polychromatic white light into a rainbow of monochromatic wavelengths (from 380 nm to 780 nm) by controlled chromatic dispersion. The measuring range is given by the distance between the apices of the triangles of the ultraviolet and red lights (see Fig. 6a). Lights of different wavelengths are reflected from the measuring object, but a system consisting of a semipermanent mirror and a pinhole ensures that only the beams of the focused wavelength are not blocked. Sensors are connected by optical fiber to another device—the controller—which contains a spectrometer. The wavelength is seen as a peak in the intensity of the spectrometer, and a linear correlation obtained by the manufacturer gives as output the distance to the measuring object.

The measuring range of confocal sensors, as well as the diameter of the cone generated by the beam, is not the same for all devices. The first limitation in the sensor selection is the distance from the sensor to the target. In the case of Layer 2, the minimum distance is the sum of Channel 3 width (6 mm), the thickness of the closed-cell foam used next to the cover (3 mm), and the thickness of the cover (4 mm) (see Fig. 3). This implies that the start of the sensor measurement range must be greater than 6+3+4=13 mm, which is the case for the Micro-Epsilon confocalDT IFS2404 (see Fig. 6b). The start of the measurement range is given by the height of the blue triangle ($\approx$ 14 mm), while the height of the red triangle represents the end of the measuring range (14+2=16 mm). The diameter of the holes is such that the entire beam passes through it. Smaller holes lead to a reduction of the intensity of the wavelength

peak in the spectrometer, which can lead to the deterioration of the accuracy.

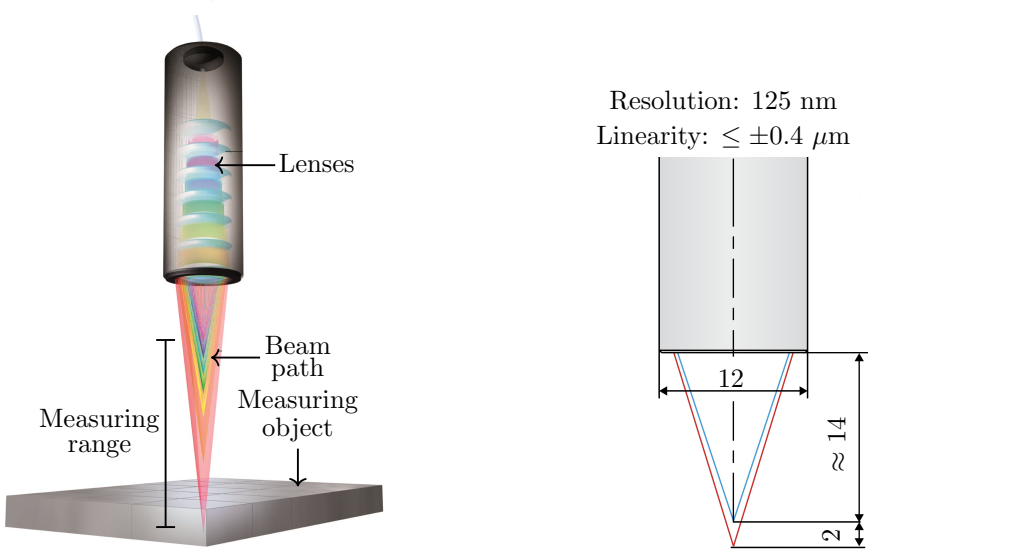

(a) Measuring principle. (b) Characteristic lengths in mm of IFS2404-2 [61].

Fig. 6: Details of confocal chromatic sensors.

The error of confocal chromatic sensors is the combination of the resolution and the linearity:

- Resolution: the smallest size that the sensor can detect. In dynamic measurements, it is higher than in static measurements. Static displacements are not considered in this work; thus, the value given in Fig. 6b is the dynamic resolution given by the official datasheet.

- Linearity: the error of the linear correlation of the distance as a function of the wavelength. Each sensor has a linearity curve that gives the deviation from the linear correlation along the measuring range (see Fig. 7). In this work, the linearity of the sensor is defined as the peak-to-peak value of this curve. This value is lower than the one given in the official datasheet (±1 µm), the maximum value among all sensors manufactured. It should be noted that linearity is defined for measurements of absolute distances of the order of the domain of Fig. 7 (from 0 to 800 µm), while the current study is focused on relative distances—with respect to the equilibrium position—of $\sim$ 1 µm. This implies that considering the sensor error to be equal to the linearity is a conservative assumption.

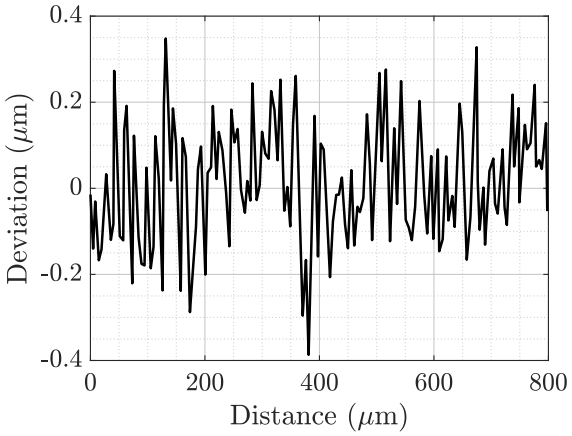

Fig. 7: Linearity curve of the IFS 2404-2 confocal chromatic sensor used for testing.

2.2. Mathematical model

In this section, the mathematical model for the fluid-structure interaction (FSI) problem for the system described in the previous section is presented.

The displacements of the layers can be divided into two parts: the static displacements produced by pressure differences in the mean flow of different channels, and the dynamic displacements generated by the pressure fluctuation due to turbulence.

In this work, steady displacements are not taken into account. This is reasonable in Channels 1, 2, and 3, since the pressure loss is dominated by the foams (see [24]), whose length is the same in all channels. In addition, the channel flow distributors shown in Fig. 3 are designed so that the pressure loss is the same in all of them, ensuring a minimum pressure difference between the channels. In Channel 0, a static structural analysis using the pressure forces obtained from the order-of-magnitude analysis of [24], including a safety factor of 5, has shown that the displacements are of the order of 10^{-4} µm, which concludes the justification that static displacements are negligible with the present geometry and flow parameters.

In terms of dynamic displacements, as discussed in the Introduction, the maximum permissible displacement for the layers is approximately 5 µm. Therefore, a decoupled Fluid-Structure Interaction (FSI) strategy remains valid provided that these displacements do not interfere with the fluid flow; specifically, if both the undeformed and deformed geometries result in identical aerodynamic forces. A standard mesh requirement for accurate LES simulations is that the dimensionless wall distance of the first near-wall cell is $\tilde{y}_w^+ \leq 1$. The wall distance of the first near-wall cell such that $\tilde{y}_w^+ \leq 1$ can be estimated using the Schlichting correlation for the skin friction coefficient of a flat plate [62]. Using the Reynolds number of 3000 mentioned in the Introduction, the estimated wall distance of the first near-wall cell such that $\tilde{y}_w^+ = 1$ is $h = 25$ µm. This value is one order of magnitude higher than the characteristic displacements, which means that the effect of structural displacements on the fluid flow can be neglected. In sum-

mary, it is justified to consider a decoupled FSI in the model, although the validity of the model is limited to small displacements as those considered in the current application. If the characteristic displacements given by this method are much higher than the sensor accuracy, then the model accuracy is reduced. However, this case is irrelevant, since the detector cannot be installed under those conditions. In this case, design improvements or the reduction of the air freestream velocity would be required to match the targets set by the ALICE experiment.

2.2.1. Fluid simulations

Equations

The incompressible filtered Navier-Stokes equations for the air are [31]:

$$\begin{cases} \nabla \cdot \boldsymbol{v} = 0 & (1) \\ \dfrac{\partial \boldsymbol{v}}{\partial t} + \boldsymbol{v} \cdot \nabla \boldsymbol{v} = -\dfrac{1}{\rho}\nabla p + \nabla \cdot [(\nu + \nu_t)\nabla \boldsymbol{v}] + \boldsymbol{S}, & (2) \end{cases}$$

where ρ is the density, $\boldsymbol{v}$ is the velocity, t is the time, p the pressure, and ν the kinematic viscosity. Eqs. (1) to (2) also contain the following assumptions, terms, and parameters:

- *Implicitly-filtered Large Eddy Simulations* are performed (see [31]). Thus, it is assumed that the finite support of the computational mesh with the low-pass characteristics of the discrete differentiating operators acts as an effective filter.

- The isotropic part of the *subgrid stress tensor* is included in the filtered pressure, and ν_t is derived from the Boussinesq assumption is provided by the WALE model [63] with the wall constant $C_w = 0.325$.

- The *momentum source term* $\boldsymbol{S}$ takes into account the pressure loss of foams [64]:

$$\boldsymbol{S} = \Phi\left(\frac{\mu}{\mathcal{P}} + \frac{\Phi\rho C_d}{\sqrt{\mathcal{P}}}|\boldsymbol{v}|\right)\boldsymbol{v}\ \mathbf{1}_{\Omega_f}. \quad (3)$$

  where $\mathbf{1}_{\Omega_f}$ is the indicator function in the foam domain. The first component (Darcy's law) represents the drag of Stokes flows ($Re \ll 1$), while the second component (Forchheimer's law) provides the general expression for $Re \gg 1$, with Φ, $\mathcal{P}$ and C_d referring to the foam porosity and permeability and drag coefficients, respectively, while μ to the air viscosity. The values are $\Phi_{K9} = 0.89$, $\Phi_{RVC} = 0.97$, $\mathcal{P}^{\mathrm{RVC}} = 3.32 \times 10^{-9}$ m^2, $\mathcal{P}^{\mathrm{K9}} = 5.97 \times 10^{-10}$ m^2, $C_d^{\mathrm{RVC}} = 7.81 \times 10^{-2}$, and $C_d^{\mathrm{K9}} = 1.02 \times 10^{-1}$ [23].

Geometry and boundary conditions

The computing power available does not allow for the performance of the fluid simulation of the entire geometry of Fig. 3. The mesh required to solve at least 80% of the turbulent kinetic

energy [31] requires a high cell count. This implies the use of a small time step, while the number of simulated time steps is high due to the large ratio between the channel length and width (280 mm/6 mm $\approx$ 50, see Fig. 8). To reduce the computational cost of the simulations, the first additional assumption consists of considering that the flow in the four channels is independent. This is equivalent to stating that there is no flow between the layers, which is the case when the longerons are considered to be walls (no air can penetrate through them), and that the gap of 1.5 mm of Fig. 3b to the symmetry plane (0.5 mm in the real ITS3, see Fig. 1b) does not exist. This assumption allows the simulation of each channel separately, reducing the computational cost of the fluid simulations.

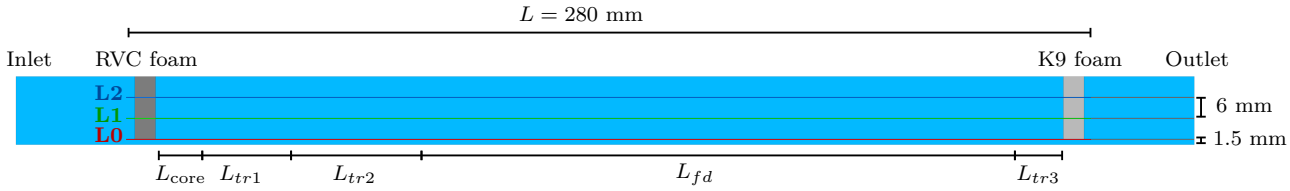

Fig. 8: Cut with the plane $y = 0$ of a half-barrel of the ALICE ITS3.

In free shear flows, turbulence is generated at much lower Reynolds numbers than in wall-bounded flows. This fact motivates the assumption that the free shear flow after the air passes through the holes of the foams is responsible for the pressure fluctuations in the silicon layers. These fluctuations begin at the potential core during the spatial development of the Kelvin-Helmholtz instability, in a region of length L_{core} (see Fig. 8). Then, fluctuations reach their maximum intensity in a region of length L_{tr1}, to then be reduced in a region of length L_{tr2}, in which the channel flow starts to develop. After a distance from the holes of $L_{\text{core}} + L_{tr1} + L_{tr2}$, the fully developed channel flow regime is reached, and this behavior holds for a distance of L_{fd}, in particular until a distance of L_{tr3} before the K9 foam, in which the flow is accelerated locally near the holes.

Considering the previous ideas, the second additional assumption consists of reducing the length of the computational domain. It is assumed that the displacements are mainly caused by the pressure fluctuations in the region of length L_{tr1}, and the computational domain extends from the inlet of Fig. 8 until the flow is fully developed at a distance to the foam of $L_{\text{core}} + L_{tr1} + L_{tr2} = L/3$. This is considered to be valid in the current application, since the $Re_h = 3000$ in the fully-developed channel flow, which is transitional, while at high Reynolds number additional verification steps would be needed. The total value of $L/3$, as well as the length of $L/10$ from the inlet to the foam (see Fig. 9b), has been derived from preliminary steady simulations using the $k-\omega$ SST RANS turbulence model [65]. Solving the fluid flow only in the relevant regions with a reduced domain is assumed to be applicable to other internal flows such as turbomachinery.

Inlet turbulence levels are assumed not to affect the downstream solution since the RVC

foam acts as a flow straightener credit to its low characteristic cell size of about 100 µm [23]. Its effect on the free shear flow generated in the holes is assumed to be similar to the error related to other assumptions of the model. In addition, since the heights of Channels 1, 2, and 3 are the same (and in Channel 0 there is no free shear flow due to the absence of foams, see Fig. 1a), it is reasonable to assume that the aerodynamic loads produced in Layer 0, Layer 1, and Layer 2 are of the same order. Since the displacements are inversely proportional to the structural stiffness, for the same aerodynamic loads in all layers, the highest displacements are expected in Layer 2. As a consequence, this work will focus only on the displacements of Layer 2, which means that only Channels 2 and 3 will be simulated, and the pressure at Layer 2 is obtained as the difference between the wall pressure obtained in the simulation of Channel 3 and the one of the simulation of Channel 2.

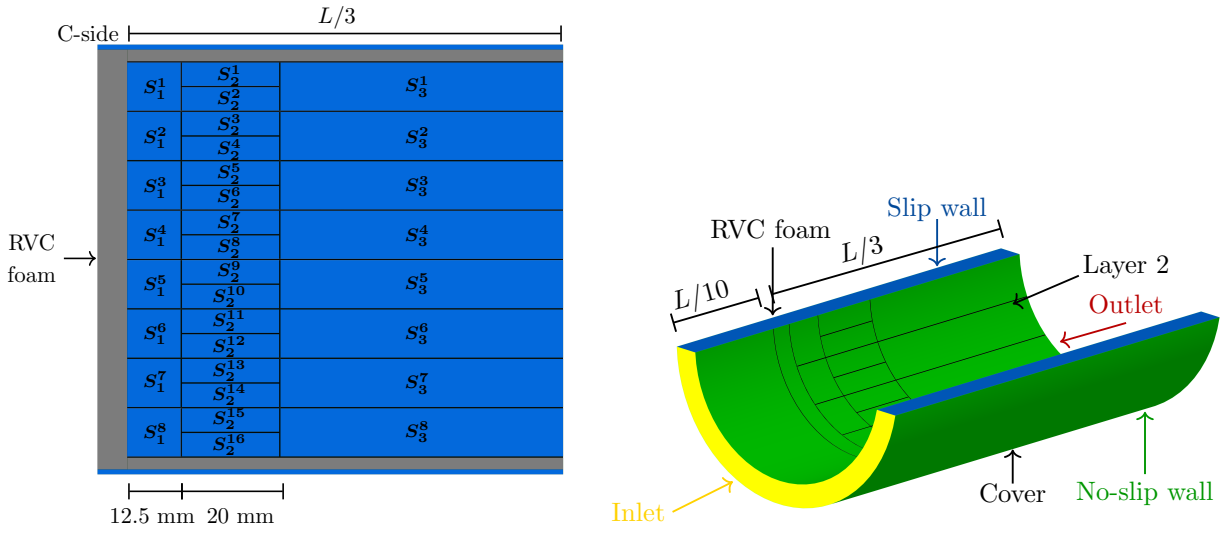

(a) Sub-surfaces of Layer 2.

(b) Isometric view of Channel 3.

Fig. 9: Geometry of the fluid simulations for the calculation of the aerodynamic forces in Layer 2.

The procedure to transfer the pressure loads obtained from fluid simulations to structural simulations is a key part of the model. Generating the same computational mesh for both simulations is discarded, since fluid simulations require a much smaller mesh size, and generating a mesh with small size for structural simulations notably increases the computational cost of these simulations. An alternative is to generate meshes of different sizes to project pressure values from the fine (fluid) mesh to the coarse (structural) mesh. However, the current situation is such that this process cannot be automated in Ansys Mechanical/Fluent, which is the software used in the current work. As a solution, a division of Layer 2 into sub-surfaces is proposed, and average values over these sub-surfaces are extracted and used as inputs for structural simulations. Considering the unbent Layer 2 for the ease of illustration, the division in the longitudinal direction is done into three sections, including a first part of length $L_{\text{core}} = 12.5$ mm (S_1), a

second part of length $L_{tr1} = 20$ mm (S_2), and a third part of length $L_{tr2} = L/3 - 20 - 12.5$ mm (S_3, see Fig. 9a). The division in the orthogonal direction is done taking as reference the number of holes of the foam (16). As mentioned previously, pressure fluctuations are expected to be dominant in the region of length $L_{tr1} = 20$ mm; therefore, S_2 sub-surface is divided into 16 additional sub-surfaces; that is, two times greater number of elements than S_1 and S_3. These divisions and lengths have been obtained from preliminary simulations with a coarse mesh.

The boundary conditions of the fluid simulations are sketched in Fig. 9b. The velocity at the inlet is set to the freestream velocity v_∞, whereas, for the outlet, the pressure is set to the reference pressure p_∞. No-slip condition is imposed in all walls of the domain except the wall in contact with the longerons, in which a slip boundary condition is applied. The same reasoning applies to the simulations of Channel 2.

Numerical implementation

Eqs. (1) to (2) are solved with the finite volume method [66] that is implemented in Ansys Fluent 2023R1 [67]. The poly-hexcore method is used for meshing, which creates a mesh consisting of octrees in the bulk region, keeps a high-quality layered poly-prism mesh in the boundary layers, and connects these two meshes with general polyhedral elements. The computational mesh is generated with two different cell sizes. The fine mesh size Δ is defined in the S_1 and S_2 surfaces (see Fig. 9a), while in S_3 the mesh size is equal to 2Δ. It has been verified in preliminary simulations that the results given by this mesh are the same as those obtained with a uniform mesh of size Δ. In the no-slip walls, the poly-prism mesh of the boundary layer is defined such that $\tilde{y}_w^+ \leq 1$ and the aspect ratio of the first near-wall cell is lower than 3.

Flow variables are stored at cell centers, and cell face values are computed with interpolation schemes. A central difference scheme is used for pressure and velocity in the momentum equation, while, in the continuity equation, a corrected momentum interpolation is proposed to avoid pressure checkerboarding [68]. Gradients are obtained using a least-squares procedure. The temporal discretization is a second-order implicit scheme, and a linearized form of each equation for the flow variable Ψ is [67]:

$$A^n_{\text{cell}}\Psi^{n+1}_{\text{cell}} = \sum_{nb} A^n_{nb}\Psi^{n+1}_{nb} + B^n_{\text{cell}}. \tag{4}$$

In Eq. (4), nb denotes neighbor cells, superindexes n and $n+1$ refer to the current and next time step, respectively, and A and B are constants. The pressure-velocity coupling is performed with the SIMPLEC algorithm [66]; in each iteration, the systems of linear algebraic equations are solved using an algebraic multigrid method that uses the Gauss-Seidel method as smoother [69]. In the m-th iteration, the globally-scaled residuals of Eq. (4) are defined as follows [67]:

$$R_{\Psi}^{m} = \frac{\sum_{\text{cell}} |\sum_{nb} A_{nb} \Psi_{nb}^{m}|}{\sum_{\text{cell}} |A_{\text{cell}} \Psi_{\text{cell}}^{m}|}. \tag{5}$$

It is verified that, at the end of the iterative process that is done every time step, the globally-scaled residuals are $< 5 \times 10^{-4}$ (continuity), $< 10^{-5}$ (momentum and turbulent variables), and $< 10^{-8}$ (energy). These values are lower than those by default in Ansys Fluent of $< 10^{-3}$ (continuity, momentum, and turbulent variables) and $< 10^{-6}$ (energy). Simulations are started at $t = t_0$ from a precursor RANS simulation (steady-state solver with second-order upwind discretization in the convective terms), and the time step is selected such that the maximum cell convective Courant number $Co < 0.5$. The same time step is used in all simulations of the mesh independence study. The simulations are completed when the flow statistics (pressure forces) reach a statistically steady state at $t = T$. Pressure forces are extracted at the same frequency as the sampling frequency of the confocal sensor (30 kHz).

2.2.2. Structural simulations

Equations

The displacements $\boldsymbol{d}$ of Layer 2 are obtained from the following equation [70]:

$$\boldsymbol{M}\frac{\partial^2 \boldsymbol{d}}{\partial t^2} + \boldsymbol{C}\frac{\partial \boldsymbol{d}}{\partial t} + \boldsymbol{K}\boldsymbol{d} = 0 \tag{6}$$

where $\boldsymbol{M}$ is the mass matrix, $\boldsymbol{C}$ is the damping matrix, and $\boldsymbol{K}$ is the stiffness matrix.

The mass and stiffness matrices are obtained from known material properties, while the damping matrix is, a priori, unknown. Rayleigh approximation is considered, in which the damping matrix is a linear function with respect to the mass and stiffness matrices [70]:

$$\boldsymbol{C} = \alpha \boldsymbol{M} + \beta \boldsymbol{K}, \tag{7}$$

with α and β referring to the mass and stiffness multipliers, respectively. These values relate the damping ratio at a particular natural frequency, ζ_i, with the natural frequency f_i [71]:

$$\zeta_i = \frac{\alpha}{4\pi f_i} + \pi \beta f_i. \tag{8}$$

The values of α and β are closed with the damping ratios of two natural frequencies of the system. The damping ratio is estimated using the half-power bandwidth method [72], which uses the experimental frequency response of the geometry under consideration as a reference. For a natural frequency f_i whose corresponding amplitude is $\hat{d}_{\max}$, then $\zeta_i = 2(b-a)/f_i$, where a and b are the frequencies such that the amplification is equal to $\hat{d}_{\max}/2$ (see Fig. 10).

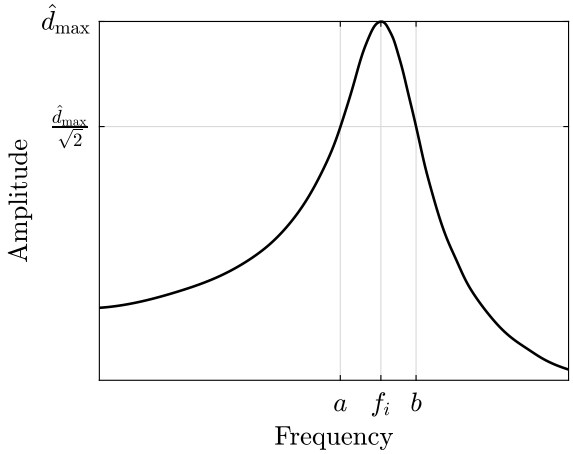

Fig. 10: Half-bandwidth method for the calculation of the damping ratio.

Geometry and boundary conditions

The geometry of the transient structural simulations is shown in Fig. 11. The entire Layer 2 is simulated, with the pressure forces obtained from the fluid simulations as boundary conditions. At the surface of length $L - L/3 = 2L/3$ —not considered in the fluid simulation—the mean value (in space) of the pressure at the S_3 sub-surfaces (see Fig. 9a) is applied, representing an approximation of the fully developed channel flow (see Fig. 8). The bonding between foams and silicon layers is assumed to be infinitely stiff; therefore, foam surfaces are fixed supports.

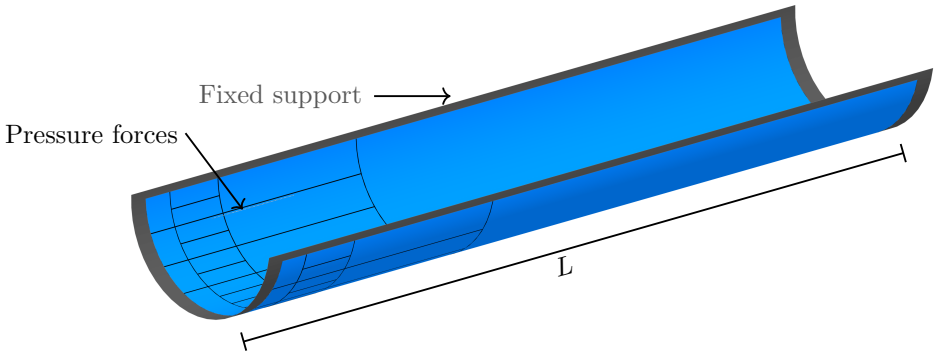

Fig. 11: Geometry and boundary conditions of the structural simulations of Layer 2.

Numerical implementation

Eq. (6) is solved with the finite element method that is implemented in Ansys Mechanical 2023R1 [73]. Since the layer thickness is negligible with respect to the other dimensions, particularly to the radius of curvature of the bent layers, shell elements are used [74]. This allows the generation of a two-dimensional mesh, in which quadrilateral elements are used with a uniform size equal to δ. In the simulations of the experimental setup, the layout explained in Section 2.1, including the glue, is taken as a reference, and the copper layer is neglected as a first approximation. This is because the copper layer has the geometry of a "serpentine"

(see Fig. 12), and the direction of the serpentine is such that the contribution to the bending stiffness of the structure in the y direction (normal to the unbent layer) is considerably reduced with respect to a fully-solid layer. The contacts between the layers of the integrated heaters are assumed to be ideal; that is, there is no separation nor sliding between the layers.

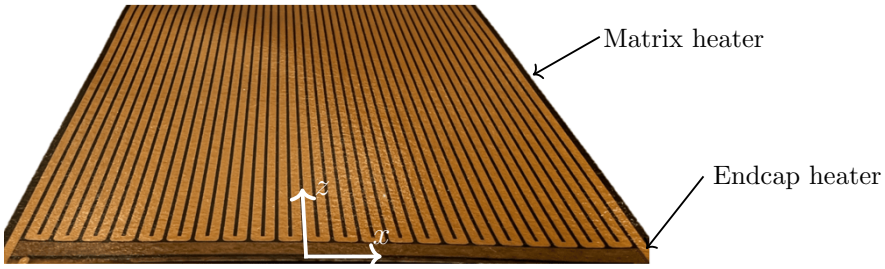

Fig. 12: Layers with integrated heaters used in the experimental setup.

The mass and stiffness matrices are given by the following integrals [70]:

$$\boldsymbol{M} = \rho \int_{S_e} \boldsymbol{N}^T \boldsymbol{N} \, \mathrm{d}\mathcal{S}, \quad \boldsymbol{K} = \int_{S_e} \boldsymbol{B}^T \boldsymbol{D} \boldsymbol{B} \, \mathrm{d}\mathcal{S}, \tag{9}$$

where ρ is the material density, S_e are the surfaces of the mesh elements, and the matrices are defined as follows [70]:

- $\boldsymbol{N}$: relates the nodal displacements $\boldsymbol{u}$ and the displacements of a general point:

$$\boldsymbol{w} = \boldsymbol{N}\boldsymbol{u}. \tag{10}$$

- $\boldsymbol{B}$: relates the strains $\boldsymbol{\varepsilon}$ to the nodal displacements:

$$\boldsymbol{\varepsilon} = \boldsymbol{B}\boldsymbol{u}. \tag{11}$$

- $\boldsymbol{D}$: the elastic stiffness matrix that relates stresses $\boldsymbol{\sigma}$ and strains:

$$\boldsymbol{\sigma} = \boldsymbol{D}\boldsymbol{\varepsilon}, \tag{12}$$

  and whose local components in the directions $\hat{x}$, $\hat{y}$, and $\hat{z}$ for an orthotropic material are [70]:

$$\begin{bmatrix} \sigma_{\hat{x}\hat{x}} \\ \sigma_{\hat{y}\hat{y}} \\ \sigma_{\hat{z}\hat{z}} \\ \sigma_{\hat{x}\hat{y}} \\ \sigma_{\hat{x}\hat{z}} \\ \sigma_{\hat{y}\hat{z}} \end{bmatrix} = \begin{bmatrix} \frac{1}{E_{\hat{x}}} & -\frac{\nu_{\hat{x}\hat{y}}}{E_{\hat{y}}} & -\frac{\nu_{\hat{x}\hat{z}}}{E_{\hat{z}}} & 0 & 0 & 0 \\ -\frac{\nu_{\hat{x}\hat{y}}}{E_{\hat{y}}} & \frac{1}{E_{\hat{y}}} & -\frac{\nu_{\hat{y}\hat{z}}}{E_{\hat{y}}} & 0 & 0 & 0 \\ -\frac{\nu_{\hat{z}\hat{x}}}{E_{\hat{z}}} & -\frac{\nu_{\hat{z}\hat{y}}}{E_{\hat{y}}} & \frac{1}{E_{\hat{z}}} & 0 & 0 & 0 \\ 0 & 0 & 0 & \frac{1}{G_{\hat{x}\hat{y}}} & 0 & 0 \\ 0 & 0 & 0 & 0 & \frac{1}{G_{\hat{x}\hat{z}}} & 0 \\ 0 & 0 & 0 & 0 & 0 & \frac{1}{G_{\hat{y}\hat{z}}} \end{bmatrix}^{-1} \begin{bmatrix} \varepsilon_{\hat{x}\hat{x}} \\ \varepsilon_{\hat{y}\hat{y}} \\ \varepsilon_{\hat{z}\hat{z}} \\ \varepsilon_{\hat{x}\hat{y}} \\ \varepsilon_{\hat{x}\hat{z}} \\ \varepsilon_{\hat{y}\hat{z}} \end{bmatrix}. \tag{13}$$

where ν, E, and G are the Poisson's ratio and Young's and shear moduli, respectively. The elastic behavior of all materials is justified from the small displacement assumption (up to 5 µm). All materials considered in this study are assumed to be isotropic except from silicon, which is orthotropic. In each point of the unbent Layer 2, following the global coordinate system shown in Fig. 2a, the $\hat{z}$ axis is defined in the along the 280 mm-length layer, the $\hat{y}$ axis in the normal direction to the layer, and the $\hat{x}$ axis such that it leads to a cartesian right-handed coordinate system (see Fig. 12).

3. Results

First the accuracy of the models developed in Section 2.2 is assessed in Section 3.1 by comparing numerical results with data obtained from the experiment described in Section 2.1. The validated model is then used to simulate the real configuration of the ITS3, as well as to study new configurations due to possible modifications in detector cooling and installation requirements in Section 3.2.

Simulation parameters are given in Table 1. Mechanical properties have been received by private communication with the suppliers of the glue and the polyimide (PI), the components of the stiffness matrix of the p-type (100) silicon wafer have been obtained from [75], and the properties of Al (used later in a parametric study) and Cu from [76]. Regarding the airflow, it has been shown in [24] that values of the freestream velocity $v_\infty > 5$ m/s are required to meet thermal design requirement. On the contrary, values of $v_\infty > 8$ m/s do not yield significant improvements in thermal performance while leading to a large pressure loss. Thus, as a realistic conservative assumption, freestream velocity is fixed at 8 m/s in all simulations. This condition is concluded to represent real conditions in which the detector could operate while meeting the thermal requirements.

Symbol	Material	Parameter	Direction	Value	Units
E	Al	Young modulus		70	GPa
	Cu			130	
	Glue			2	
	PI			2.4	
	Si		x	169	
	Si		y	130	
	Si		z	169	
G	Si	Shear modulus	xy	79.6	GPa
	Si		xz	50.9	
	Si		yz	79.6	
v_∞	Air	Freestream velocity	z	8	m/s
γ	Al	Poisson ratio		0.33	
	Cu			0.36	
	Glue			0.33	
	PI			0.34	
	Si		xy	0.28	
	Si		xz	0.064	
	Si		yz	0.36	
μ	Air	Viscosity		1.837×10^{-5}	$\mathrm{Pa} \cdot \mathrm{s}$
ρ	Al	Density		2700	$\mathrm{kg/m^3}$
	Cu			8960	
	Air			1.184	
	Glue			1150	
	PI			1420	
	Si			2329	

Table 1: Simulation parameters.

3.1. Model validation

The first steps of the model validation are carried out in Section 3.1.1 with mesh independence studies performed in fluid and structural simulations. The selection of correct meshes allows the comparison with experimental data obtained with confocal sensors in Section 3.1.2. Finally, the effect of an assumptipon done in the model regarding the modeling of the integrated heaters of the experimental protoytype is assessed in Appendix A.

3.1.1. Mesh independence studies

The first study is done in the fluid simulations. Since there are no relevant mean quantities of interest in the flow, the study will be focused on the spectral content. The time history of the pressure $p = p(t)$ is extracted from $t = 0$ to $t = T$ on the surfaces S_1^4, S_2^8, and S_3^4 (see Fig. 9a), and the variance of the signal $\sigma^2(p(t))$ is used as a convergence indicator [77]. The value $\sigma^2(p_i^j)$ will be referred to S_i^j. The consideration of the variance is because the power spectral density (PSD), S_{pp}, will be analyzed in the comparison with experimental data, and both variables are related in the frequency domain as follows:

$$\sigma^2(p) = \int_0^\infty S_{pp}(f)\ \mathrm{d}f - \mu(p)^2, \tag{14}$$

where μ is the mean value of $p(t)$, and S_{pp} represents the signal power:

$$S_{pp}(f) = \frac{1}{T}|\hat{p}(f)|^2 = \frac{1}{T}\left|\int_0^\infty p(t)e^{-2\pi i f t}\ \mathrm{d}t\right|^2, \tag{15}$$

with $\hat{p}(f)$ referring to the Fourier transform of the function $p = p(t)$.

Three meshes of different sizes are considered in the simulations, which are referred to the channel height h in Table 2. The study is conducted only in Channel 3, given the similarities between the geometries of Channels 2 and 3 (see Fig. 3). The results show that the differences between the variance values decrease as the size of the mesh decreases, leading to convergent behavior. The mesh of 15.7 M of cells is considered for the following simulations, in which the aspect ratio of the first near-wall cell is 2.5 to achieve $\tilde{y}_w^+ = 1$, which is acceptable for LES simulations.

$\boldsymbol{\Delta_{\min}}$	**Number of cells**	$\boldsymbol{\sigma^2(p_1^4)}$ **(Pa²)**	$\boldsymbol{\sigma^2(p_2^8)}$ **(Pa²)**	$\boldsymbol{\sigma^2(p_3^4)}$ **(Pa²)**
$h/25$	2.8 M	0.099	0.282	0.026
$h/37.5$	5.4 M	0.128	0.349	0.027
$h/50$	15.7 M	0.141	0.387	0.027

Table 2: Results of the mesh independence study of the fluid simulations of Channel 3.

The variances obtained prove that pressure fluctuations are dominant in the S_2 surfaces, and that the effect of the periodic channel flow (S_3) on the displacements of Layer 2 is negligible. These results support the assumption of reducing the length of the fluid domain.

Using the pressure forces obtained from the fluid simulations performed with the fine mesh, structural simulations have been performed. Three mesh sizes are considered, and the first natural frequency obtained from a modal analysis (f_1) and the peak to peak value of the

displacements at the center point (d_{p-p}^{center}) are used for result comparison. Table 3 shows that a convergent behavior is achieved, and the mesh of $\delta = h/6$ is used for the structural simulations.

$\boldsymbol{\delta}$	**Number of cells**	$\boldsymbol{f_1}$ **(Hz)**	$\boldsymbol{d_{p-p}^{\text{center}}}$ **(μm)**
h	0.9 K	660	0.6
$h/2$	2.9 K	599	0.35
$h/6$	25 K	586	0.3

Table 3: Results of the mesh independence study of the structural simulations of Layer 2.

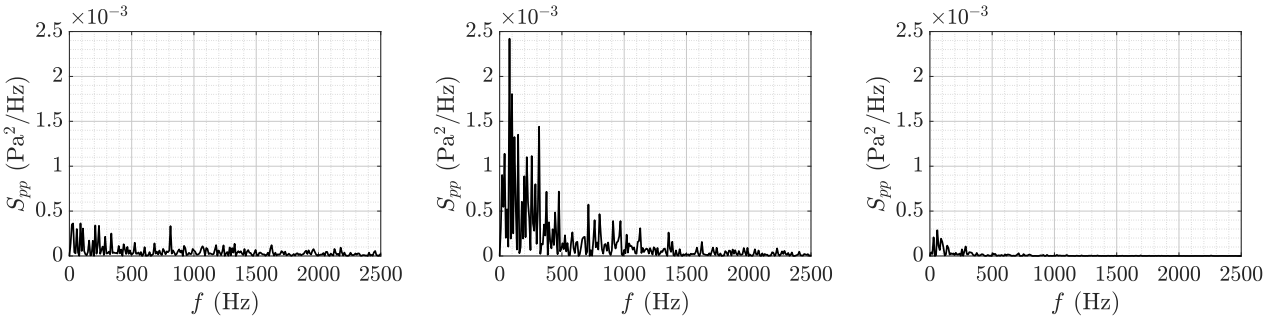

(a) S_1^4. (b) S_2^8. (c) S_3^4.

Fig. 13: Power spectral densities of the pressure on Layer 2 obtained from Channel 3 simulation.

3.1.2. Comparison with experimental data

Fig. 14a compares the PSDs given by the confocal sensor and the mathematical model developed in this work at the center point. This graphical representation provides the response of the system and gives the relevance of the natural frequencies of the system, which make it a crucial variable to determine the structural behavior of the particle detector. The model provides the main peak at 586 Hz in the simulation, while in the experiments it is approximately at 550 Hz. The high accuracy confirms the validity of the assumption done on the modeling of the layout of the integrated heaters (see Appendix A). The peak corresponds to the first natural frequency of Layer 2 of the prototype. This claim can be verified in Fig. 15a, in which only the natural frequencies with displacements in least one of the two measurement points are illustrated. These contours are essential for the identification of the peaks of the PSDs with natural frequencies of the system. The model also predicts significant contributions of the eighth and twelfth natural frequencies (see Figs. 15c and 15d). The former is also present at approximately the same frequency in the experiments, but with decreased amplitude, while the latter is not identified. As expected, the smallest contribution is given by the fifth natural frequency, given that the displacement at the center point is negligible (see Fig. 15b). Since the

dominant frequencies of the aerodynamic forces are lower than the first natural frequency (see Fig. 13), the risk of failure of the system due to mechanical resonance is reduced.

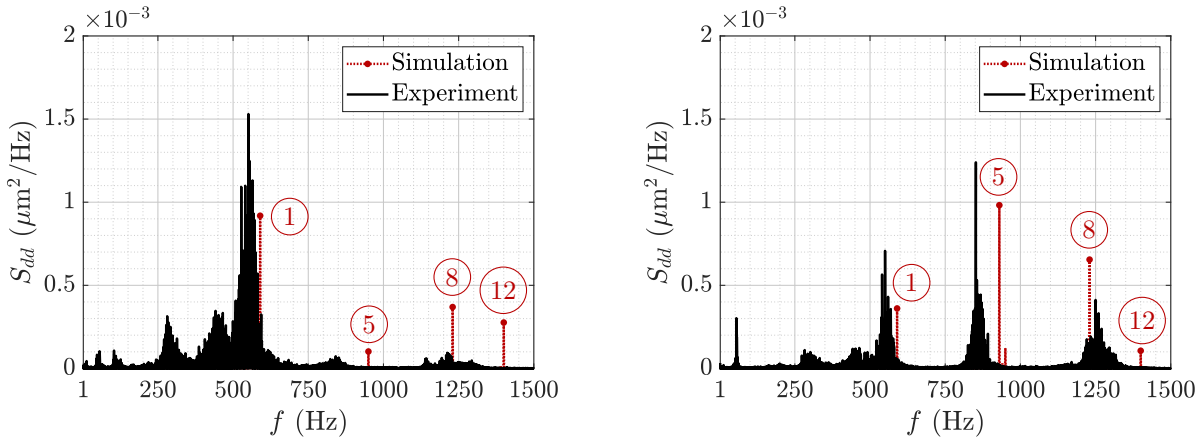

(a) Center point.

(b) C-side point.

Fig. 14: Power spectral densities of Layer 2 displacements of the experimental setup obtained from experiment and simulation. Peaks related to natural frequencies are indicated with numbers.

The displacement PSDs obtained at the C-Side point are given in Fig. 14b. In both approaches the most relevant contribution is given by the fifth natural frequency, while the peak of the first and eighth natural frequencies is of the same order of magnitude. In the same way as at the center point, the simulation predicts a peak at approximately 1400 Hz that is not noticed in the experiments. Moreover, a mode appears at 55 Hz with reduced damping in the experiments, which is not present in the simulation. Since this value is much lower than the first natural frequency of the layer, it is assumed that this is a part of the vibrations of the whole wind tunnel due to external noise. Indeed, multiples of 55 Hz are also identified at the center point (275 Hz and 440 Hz). This is a characteristic behavior of structures connected mechanically to engines [78], which is the case in the current experimental setup (see Fig. 4). Given that the displacement of the surrounding structure of the prototype does not vanish, it is expected that the experiment overpredicts the values of the displacements of the layers. To determine the damping coefficients (Eq. (7)), experimental data at the C-side point (fifth natural frequency) and at the center point (first natural frequency) have been used, leading to a value of $\zeta = 0.001$ for both natural frequencies, which in turn is equivalent to $\alpha = 4.19$ and $\beta = 2.2 \times 10^{-7}$.

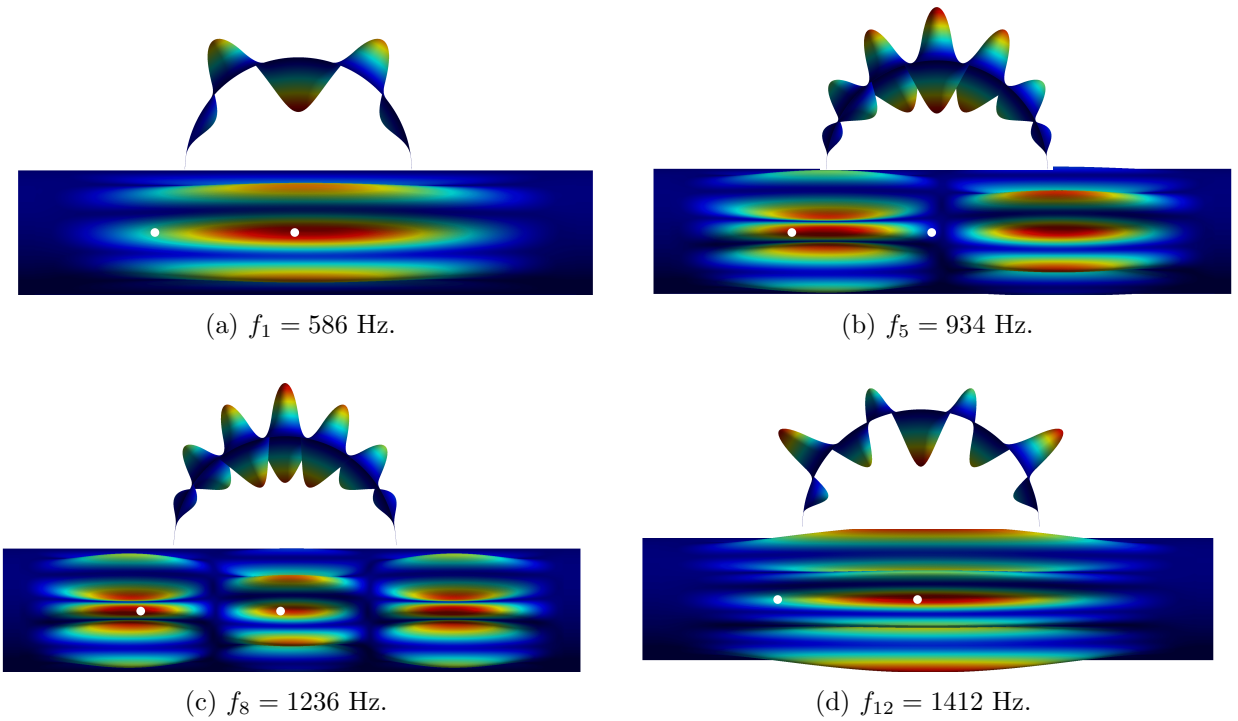

(a) $f_1 = 586$ Hz. (b) $f_5 = 934$ Hz.

(c) $f_8 = 1236$ Hz. (d) $f_{12} = 1412$ Hz.

Fig. 15: Side and top view of the natural frequencies of Layer 2 of the experimental setup with relevant displacement in the measurement points. These points are highlighted in white bullets.

Figure 16 shows the time histories of the PSDs of Fig. 14a during one second, the simulation time in which the displacement values are extracted. The simulations provide a peak-to-peak value $d_{p-p}^{\text{center}} \approx 0.3$ µm, while, in the experiments, $d_{p-p}^{\text{center}} \approx 1$ µm. As anticipated in the previous paragraph, the main reason is that the displacements of the entire wind tunnel are responsible for the contributions for $f < 550$ Hz and possibly for higher frequencies. Another important aspect is the damping term of Eq. (6). In the experimental data of Fig. 14b, the peaks at the natural frequencies are approximately a Dirac delta for values of the PSD higher than the peak value divided by $\sqrt{2}$, which is the limit value used in the half-power bandwidth method. This also occurs in the simulations. However, the contribution of the natural frequencies for which the value of the PSD is lower than the limit is negligible in the simulation, leading to low bandwidth; in the experiments the bandwidth is significantly large (see the zoom of Fig. 14b). Apart from the limitations of the modeling approach, it cannot be ruled out that the structure of the entire wind tunnel has a damping ratio much higher than the one of the silicon layer, which would explain the experimental results. In addition, it should be noted that the resolution of the sensors (0.125 μm) is of the same order as the differences between experimental and numerical results, and the linearity (± 0.4 μm) adds additional error. Without airflow, the displacements measured by the sensor are $d_{p-p}^{\text{center}} \approx 0.2$ μm, due to a combination of sensor error and external noise in the test room.

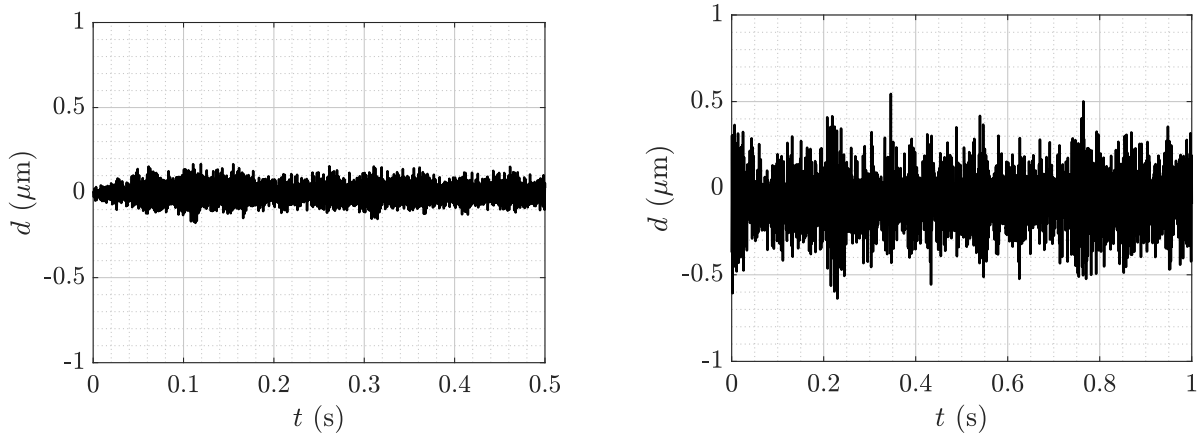

(a) Simulation.

(b) Experiment.

Fig. 16: Time history of the displacements of Layer 2 of the experimental setup at the center hole.

3.2. Real configuration

After confirming the accuracy of the mathematical model using experimental results obtained in a prototype, in this section the expected real configuration of the future ITS3 is studied. This real configuration differs from the one of the prototype in the materials used in the layers. In addition, possible adjustments required due to changes in detector cooling and installation requirements are also investigated in Section 3.2.1.

The Si layers used in the ALICE ITS3 will not contain the integrated heaters used in the experimental setup. The reference design for the real detector uses Si layers of 40 µm of thickness, although other alternatives are under consideration if that thickness cannot be achieved in the design for performance reasons: these include Si layers of 50 µm, or Si layers of 40 µm with an additional Al layer of 10 µm deposited with physical vapor deposition. Using the model developed in this work, the aerodynamic loads are the same as those obtained in the simulations of the experimental prototype, but the setup of the structural simulation changes.

Layout	$\boldsymbol{d_{p-p}^{\text{center}}}$ **(µm)**	$\boldsymbol{d_{p-p}^{\text{cside}}}$ **(µm)**	$\boldsymbol{f_1}$ **(Hz)**	$\boldsymbol{f_5}$ **(Hz)**	$\boldsymbol{f_8}$ **(Hz)**	$\boldsymbol{f_{12}}$ **(Hz)**
Si 40 µm (baseline)	0.5	0.5	766	1209	1551	1752
Si 50 µm	0.35	0.35	861	1355	1816	2074
Si+Al (40+10 µm)	0.55	0.55	761	1192	1592	1828

Table 4: Natural frequencies and displacements of Layer 2 of the real ALICE ITS3 for different layouts.

Table 4 shows the natural frequencies and displacements for different layouts. As predicted from the theory of rectangular plates [74], for a given material and planar dimensions, the natural frequencies are proportional to the thickness, which leads to the increase of the values for thicker layers. Given the similar density of Al and Si, the system mass remains approximately

constant in the Si+Al layout as opposed to the Si case of 50 µm. However, t stiffness decreases due to the significantly lower Young modulus of Al. Similar conclusions can be extracted from the displacements, with maximum differences of up to 40% between the layouts considered.

The frequency response of Layer 2 for the baseline layout is given in Fig. 17; only the first natural frequency is present in Fig. 17a, while the first and fifth frequencies are responsible for the C-side point displacements (Fig. 17a). The reduced number of relevant frequencies is because of the eighth and twelfth natural frequencies are higher than 1500 Hz, and in this range, the amplitudes of pressure forces are negligible (see Fig. 13b). The shape of the PSD and the values of the displacements are similar to those of the experimental setup, which means that the results obtained with experimental setup are representative of the real behavior of the ALICE ITS3. The design requirement ($d_{p-p} < 2$ µm) is met for all cases.

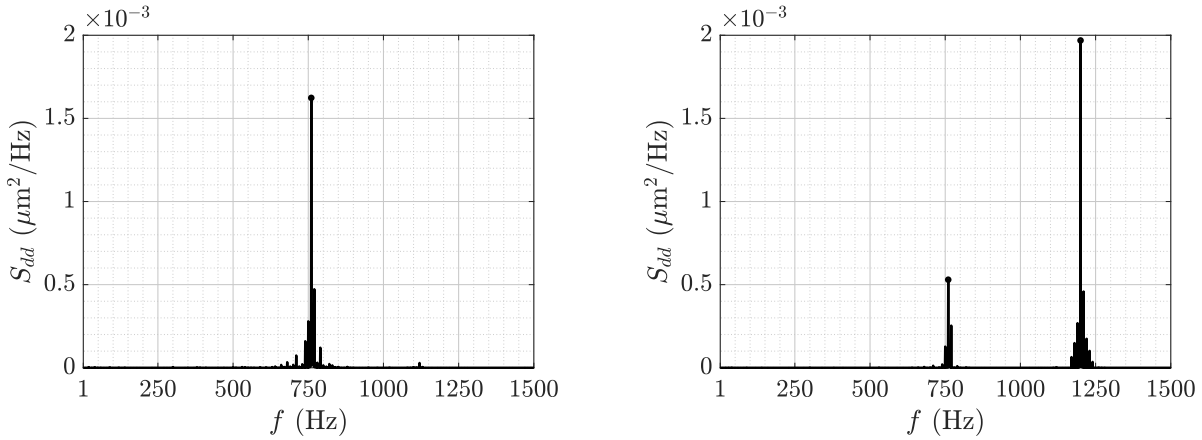

(a) Center point.

(b) C-side point.

Fig. 17: Simulation results of of Layer 2 displacements of the baseline layout of the ALICE ITS3.

3.2.1. Design modifications

As mentioned in Section 2.1, holes of 1.5 mm of diameter are drilled in the foams of the experimental setup to reduce the pressure loss. This aspect is relevant for two reasons: first, the system will work without interruption for many months, and the power consumption of the fan should be minimized; second, because the gap of 1 mm between the half-barrels (see Fig. 1b) will lead to a loss of airflow to the environment that increases as the foam pressure loss increases. Moreover, the ALICE ITS3 installation will be challenging due to the reduced free space in the ALICE cavern and the tight design tolerances; therefore, this gap could be increased up to 2 mm, leading to further increase of the leak rate. To reduce the foam pressure loss, two modifications are proposed: increasing the diameter of the hole to 2 mm (Fig. 18b) and generating 1.5 mm height slots (Fig. 18c). It has been verified that these modifications applied to the K9 foam lead to an increase of up to 1 °C at the surface in contact with the foam, and thermal design requirements [24] are met even with this increase.

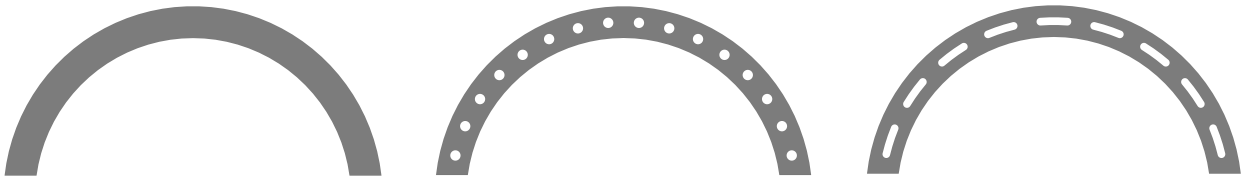

(a) No holes/slots. (b) Holes (diameter 2 mm). (c) Slots (height 1.5 mm).

Fig. 18: Different foam designs used for simulation.

Table 5 lists the foam pressure loss of different designs, which is related to the power consumption and the leak rate of the system, as well as the peak-to-peak displacements at the center and C-side point, which are required to verify that the system meets the requirements required by the organization. It is shown that drilling holes of 2 mm and slots of 1.5 mm decrease the pressure loss through the foam $(\nabla p)_f$ 15% and 30%, respectively, compared to the baseline design. However, the displacements of the layers increase significantly. In these configurations, even if the maximum velocity is reduced with respect to the baseline case (holes of 1.5 mm), the amount of air that passes through the foam cells is reduced. Since the foam acts as a turbulence reducer due to the low cell characteristic cell size ($\approx$ 200 µm), turbulence levels increase as foam material is removed. If no material is removed from the foam, no turbulence is generated, and vibrations are negligible in a channel flow at a Reynolds number of 3000. However this configuration entails a higher pressure loss than the baseline setup. It should be noted that decreasing the ratio between the foam (filled with cells) sectional area and the channel section, $\mathcal{S}$, does not lead to increased structural displacements for all values of $\mathcal{S}$. This is because in the limit $\mathcal{S} \to 0$ the foam is no longer present, and the flow is the same channel flow that leads to almost vanishing layer displacements mentioned before. These cases for which $\mathcal{S} \ll 1$ are not considered due to the fragility of foams and the compromised thermal performance. However, intermediate cases could be considered if the thermal design requirements are relaxed.

Design	$(\nabla p)_f$ **(Pa/mm)**	d_{p-p}^{center} **(µm)**	d_{p-p}^{cside} **(µm)**
Holes 1.5 mm (baseline)	110	0.5	0.5
Holes 2 mm	90	0.7	0.7
Slots 1.5 mm	75	1	1
No holes and/or slots	130	≈ 0	≈ 0

Table 5: Foam pressure loss and Layer 2 displacements of the baseline layout of the ALICE ITS3 for different foam designs.

Figure 19 illustrates the turbulent structures obtained from iso-surfaces of the Q-criterion, which is one of the invariants of the $\nabla \boldsymbol{v}$ tensor [79]. As predicted in the model developed in Section 2.2.1, the flow instability is generated after the air passes through the holes, and the size

of the turbulent region is of the order of the hole diameter in S_1 as defined in Fig. 9a. This leads to no interaction with Layer 2, and, as a consequence, to negligible pressure fluctuations (see Fig. 19a). Then, in S_2 the turbulent length scale increases and the jet mixing leads to maximum turbulence levels. After this point, turbulent structures are damped, giving rise downstream to the fully developed channel flow. The picture is similar in the case of 2 mm holes (Fig. 19b), with increased pressure fluctuations due to the increased amount of air that is accelerated.

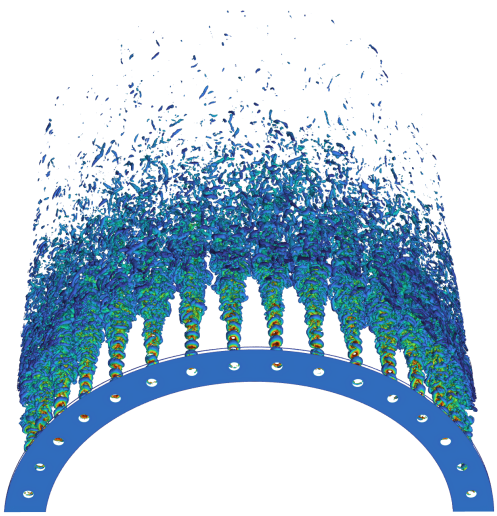

(a) Baseline (Holes, diameter 1.5 mm).

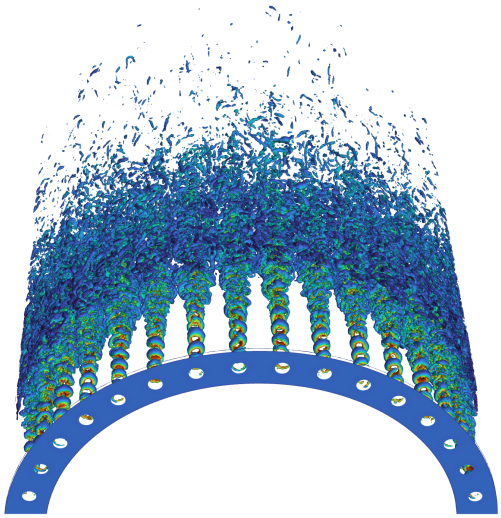

(b) Holes (diameter 2 mm).

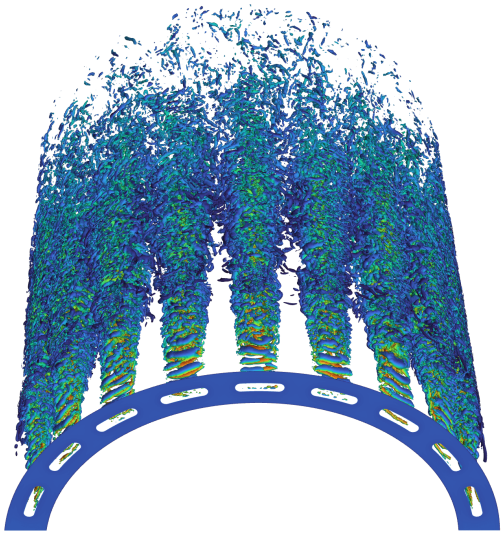

(c) Slots (height 1.5 mm).

(d) No holes and/or slots.

Fig. 19: Iso-surfaces of $Q = 5 \times 10^7$ s^{-2} for different foam designs.

The large turbulent scales provide the dominant contribution to the turbulent kinetic energy [31]; thus, higher displacements are obtained in the case with slots (see Fig. 19c). Another consequence of the higher energy of the jets is that the interaction and subsequent damping are produced further away from the foam. When no holes and/or slots are defined, there are

no turbulence sources (see Fig. 19d), and consequently, layer displacements vanish. It has been verified that the PSDs of the pressure forces of different foam designs on the surface with the highest fluctuations (S_2) are essentially Fig. 13b scaled by a factor, that is, with similar dominant frequencies. Another deduction is that the peak-to-peak values of the displacements are proportional to the peak-to-peak values of the pressure forces, which is in line with the predictions of classical analytical theories that consider steady variables [74].

4. Conclusions

In this work, the aeroelastic study of the ALICE Inner Tracking System 3 (ITS3) has been performed. This is a future particle detector of the ALICE experiment that will consist of three silicon layers of approximately 40 µm of thickness that will be bent into half-cylindrical shape. The detector will use a cooling system based on air convection to remove the heat dissipated by the layers, which will be the first time in the Large Hadron Collider. The structure will contain carbon foams as structural supports and heat exchangers, leading to an extremely low value of the material budget, which is one of the performance indicators of particle detectors.

The interaction between the airflow and the silicon layers has been studied experimentally and numerically. The displacement of the outermost layer of a prototype of the ITS3 has been measured with a confocal sensor. This is a non-invasive device that provides sub-micron accuracy, one order of magnitude higher than industry-standard devices such as laser displacement sensors. To the authors' knowledge, this is the first publication on the use of confocal sensors in a high-level engineering application. Experimental work has been complemented with a novel model development specifically designed for analyzing the fluid-structure interaction. This model is based on decoupling the structural and fluid problems, and a geometry of reduced size focused on solving the main flow physics is defined in the fluid simulations to reduce the computational cost.

The capabilities of confocal sensors for measuring displacements with submicron accuracy and at sampling frequencies of up to 30 kHz has been demonstrated in a case of practical application. Experimental and simulation results of layer displacements have been compared in a prototype of the ITS3. It has been shown that the developed model predicts the natural frequencies identified experimentally with an error lower than 10%, and that the risk of mechanical resonance is low due to the lack of aerodynamic coupling. The results demonstrate that the model gives an accurate prediction of the peaks of the displacement spectrum. It has been noted that experimental data provide higher peak-to-peak values of the displacements than the simulations. This has been mainly attributed to the presence of low-frequency components in the experimental spectrum produced by the fan that generates the airflow. Simulations have also been performed to analyze the real configuration of the ALICE ITS3, which differs slightly from

the one used in the experimental setup. These results have demonstrated that the experimental setup is representative of the real behavior of the ALICE ITS3, and that design requirements are met in all cases considered. Parametric studies have been performed to analyze the effect of the ITS3 layer composition and thickness on the structural response. In addition, it has been concluded that foam design can be tuned to find the required balance between structural displacements, energy consumption, and detector cooling.

The current study has led to the conclusion that the external noise contributes to layer displacements of the same order as the one of the aerodynamic loads. When installed in the ALICE detector, the ITS3 will be mechanically connected to other components, which are not considered in the prototype tested in this work. The external noise of the ALICE cavern could lead to displacements of the entire structure, which would imply additional displacements of the layers. Thus, future work will deal with the modeling of noise and structural properties of the ITS3 when integrated into other subsystems of the ALICE detector.

Appendix A. Influence of the modeling of integrated heater layout

The proposed model gives an acceptable approximation of the first measured natural frequencies, with differences lower than 10% (see Table A.6). Neglecting the Cu layer is an intermediate assumption, as contributions to the mass, damping, and stiffness matrices are neglected. Even if the thickness of the copper layer is only 5 μm, the high density of this material (see Table 1) leads to a vital contribution to the system mass. Consequently, it is crucial to study the influence of the modeling assumption. The most conservative approach is to consider that Layer 2 consists of a Si layer of 40 µm and a uniformly distributed mass equal to the sum of the contributions of the glue, PI, and Cu layers. Contrarily, the ideal situation occurs when the Cu layer is added to the baseline layout. Table A.6 shows that the baseline configuration provides the closest prediction to the experimental data in the natural frequencies. In addition, the effects of modifying the layout on the values of the natural frequencies are significant, with differences up to 50% in f_1 between the Si + mass and Baseline + Cu. As expected, when only the Si layer contributes to the system stiffness, displacements increase.

Layout	$\boldsymbol{d_{p-p}^{\text{center}}}$ **(μm)**	$\boldsymbol{d_{p-p}^{\text{cside}}}$ **(μm)**	$\boldsymbol{f_1}$ **(Hz)**	$\boldsymbol{f_5}$ **(Hz)**	$\boldsymbol{f_8}$ **(Hz)**	$\boldsymbol{f_{12}}$ **(Hz)**
Experiment	1	0.9	550	850	1250	–
Baseline	0.3	0.3	586	934	1236	1412
Si + mass	0.45	0.45	438	692	888	1003
Baseline + Cu	0.2	0.2	709	1091	1452	1798

Table A.6: Natural frequencies and displacements of Layer 2 of the experimental setup for different layouts.

References

[1] A. Powell. On the Fatigue Failure of Structures due to Vibrations Excited by Random Pressure Fields. *The Journal of the Acoustical Society of America*, 30(12):1130–1135, 1958. DOI: 10.1121/1.1909481.

[2] Ronny R. and Jenny N. Imbalance estimation without test masses for wind turbines. *Journal of Solar Energy Engineering*, 131(1), 2009. DOI: 10.1115/1.3028042.

[3] P. Rolek, S. Bruni, and M. Carboni. Condition monitoring of railway axles based on low frequency vibrations. *International Journal of Fatigue*, 86:88–97, 2016. DOI: 10.1016/j.ijfatigue.2015.07.004.

[4] R. Grega, J. Krajňák, L. Žuľová, G. Fedorko, and V. Molnár. Failure analysis of driveshaft of truck body caused by vibrations. *Engineering Failure Analysis*, 79:208–215, 2017. DOI: 10.1016/j.engfailanal.2017.04.023.

[5] C. F. Ng and C. K. Hui. Low frequency sound insulation using stiffness control with honeycomb panels. *Applied Acoustics*, 69(4):293–301, 2008. DOI: 10.1016/j.apacoust.2006.12.001.

[6] D. J. Thompson. A continuous damped vibration absorber to reduce broad-band wave propagation in beams. *Journal of Sound and Vibration*, 311(3):824–842, 2008. DOI: 10.1016/j.jsv.2007.09.038.

[7] J. Yang, S. S. Sun, H. Du, W. H. Li, G. Alici, and H. X. Deng. A novel magnetorheological elastomer isolator with negative changing stiffness for vibration reduction. *Smart Materials and Structures*, 23(10), 2014. DOI: 10.1088/0964-1726/23/10/105023.

[8] S. Hauser, M. Robertson, A. Ijspeert, and J. Paik. JammJoint: A Variable Stiffness Device Based on Granular Jamming for Wearable Joint Support. *IEEE Robotics and Automation Letters*, 2(2):849–855, 2017. DOI: 10.1109/LRA.2017.2655109.

[9] E. H. Dowell and K. C. Hall. Modelling of Fluid-Structure Interaction. *Annual Review of Fluid Mechanics*, 33(1):445–490, 2001. DOI: 10.1146/annurev.fluid.33.1.445.

[10] R. L. Campbell and E. G. Paterson. Fluid–structure interaction analysis of flexible turbomachinery. *Journal of Fluids and Structures*, 27(8):1376–1391, 2011. DOI: 0.1016/j.jfluidstructs.2011.08.010.

[11] H. Zhang, L. Liu, M. Dong, and H. Sun. Analysis of wind-induced vibration of fluid–structure interaction system for isolated aqueduct bridge. *Engineering Structures*, 46:28–37, 2013. DOI: 10.1016/j.engstruct.2012.07.019.

[12] R. L. Bisplinghoff, H. Ashley, and R. L. Halfman. *Aeroelasticity*. Courier Corporation, 2013.

[13] B. Stanford S. Townsend, R. Picelli and H. A. Kim. Structural Optimization of Platelike Aircraft Wings Under Flutter and Divergence constraints. *Progress in Aerospace Sciences*, 56(8), 2019. DOI:10.2514/1.J056748.

[14] E. Jonsson, C. Riso, C. A. Lupp, C. E. S. Cesnik, J. R. R. A. Martins, and B. I. Epureanu. Flutter and post-flutter constraints in aircraft design optimization. *Progress in Aerospace Sciences*, 109(100537), 2019. DOI: 10.1016/j.paerosci.2019.04.001.

[15] S. Lawson, D. Greenwell, and M. K. Quinn. Characterisation of buffet on a civil aircraft wing. In *54th AIAA Aerospace Sciences Meeting*, 2016. DOI: 10.2514/6.2016-1309.

[16] F. J. Mangiarotti, G. Willering, L. Fiscarelli, M. Bajko, L. Bottura, V. Desbiolles, et al. Power test of the first two HL-LHC insertion quadrupole magnets built at CERN. *IEEE Transactions on Applied Superconductivity*, 32(6):1–5, 2022. DOI: 10.1109/TASC.2022.3157574.

[17] N. R. Brooks, L. Bottura, J. G. Perez, O. Dunkel, and L. Walckiers. Estimation of mechanical vibrations of the LHC fast magnetic measurement system. *IEEE Transactions on Applied Superconductivity*, 18(2):1617–1620, 2008. DOI: 10.1109/TASC.2008.921296.

[18] M. Guinchard, M. Cabon, C. Charrondière, K. Develle, P. Fessia, L. Lacny, et al. Investigation and estimation of the LHC magnet vibrations induced by HL-LHC civil engineering activities. In *Proceedings of the 9th International Particle Accelerator Conference*, 2018. DOI: 10.18429/JACoW-IPAC2018-WEPMF080.

[19] B. Di Girolamo, J. A. Boudagov, M. V. Lyablin, and S. Vlachos. The precision laser inclinometer. In *Proceedings of the 12th International Particle Accelerator Conference*, 2021. DOI: 10.18429/JACoW-IPAC2021-WEPAB281.

[20] F. Zhang, G. Blanchot, S. Higginbotham, A. Honma, A. Kalogeropoulos, M. Kovacs, et al. Prototyping and qualification of 2S modules for the CMS Outer Tracker upgrade at the HL-LHC. *Journal of Instrumentation*, 17, 2022. DOI: 10.1088/1748-0221/17/05/C05019.

[21] G. Vallone, E. Anderssen, D. N. Boettcher, T. Claybaugh, M. Janda, and K. L. Veale. Mechanical Vibrations of the ATLAS ITk Structures Under Transportation Loads. In *Forum on Tracking Detector Mechanics*, 2023.

[22] H. Kolanoski and N. Wermes. *Particle Detectors: Fundamentals and Applications*. Oxford University Press, 2020.

[23] A. Amatriain, C. Gargiulo, and G. Rubio. Numerical and experimental study of open-cell foams for the characterization of heat exchangers, 2023. DOI: 10.1016/j.ijheatmasstransfer.2023.124701.

[24] A. Amatriain, M. Angeletti, C. Gargiulo, and G. Rubio. Development of an air cooling system with low material budget for high-energy physics applications. *Applied Thermal Engineering*, 236(121699), 2024. DOI: 10.1016/j.applthermaleng.2023.121699.

[25] M. Glück, M. Breuer, F. Durst, A. Halfmann, and E. Rank. Computation of fluid–structure interaction on lightweight structures. *Journal of Wind Engineering and Industrial Aerodynamics*, 89(14):1351–1368, 2001. DOI: 10.1016/S0167-6105(01)00150-7.

[26] Z. Tong, Y. Zhang, Z. Zhang, and H. Hua. Dynamic behavior and sound transmission analysis of a fluid–structure coupled system using the direct-BEM/FEM. *Journal of Sound and Vibration*, 299(3):645–655, 2007. DOI: 10.1016/j.jsv.2006.06.063.

[27] M.S.H. Al-Furjan, M. A. Oyarhossein, M. Habibi, H. Safarpour, and D. W. Jung. Frequency and critical angular velocity characteristics of rotary laminated cantilever microdisk via two-dimensional analysis. *Thin-Walled Structures*, 157(107111), 2020.

[28] X. He, J. Ding, M. Habibi, H. Safarpour, and M. Safarpour. Non-polynomial framework for bending responses of the multi-scale hybrid laminated nanocomposite reinforced circular/annular plate. *Thin-Walled Structures*, 166(108019), 2021. DOI: 10.1016/j.tws.2021.108019.

[29] M.S.H. Al-Furjan, M. A. Oyarhossein, M. Habibi, H. Safarpour, D. Won Jung, and A. Tounsi. On the wave propagation of the multi-scale hybrid nanocomposite doubly curved viscoelastic panel. *Composite Structures*, 255(112947), 2021. DOI: 10.1016/j.compstruct.2020.112947.

[30] Z. Liu, S. Su, D. Xi, and M. Habibi. Vibrational responses of a MHC viscoelastic thick annular plate in thermal environment using GDQ method. *Mechanics Based Design of Structures and Machines*, 50(8):2688–2713, 2022. DOI: 10.1080/15397734.2020.1784201.

[31] S. B. Pope. *Turbulent Flows*. Cambridge University Press, 2000.

[32] M. Lahooti, Y. Bao, D.Scott, R. Palacios, and S. J. Sherwin. LES/DNS fluid-structure interaction simulation of non-linear slender structures in *Nektar++* framework. *Computer Physics Communications*, 282(108528), 2023. DOI: 10.1016/j.cpc.2022.108528.

[33] A. Otter, J. Murphy, V. Pakrashi, A. Robertson, and C. Desmond. A review of modelling techniques for floating offshore wind turbines. *Wind Energy*, 25(5):831–857, 2022. DOI: 10.1002/we.2701.

[34] Aitor Amatriain, Corrado Gargiulo, and Gonzalo Rubio. Generalized wall-modeled large eddy simulation model for industrial applications. *Physics of Fluids*, 36(015141), 2024. DOI: 10.1063/5.0180690.

[35] B. Šekutkovski, I. Kostić, A. Simonović, P. Cardiff, and V. Jazarević. Three-dimensional fluid–structure interaction simulation with a hybrid RANS–LES turbulence model for applications in transonic flow domain. *Aerospace Science and Technology*, 49:1–16, 2016. DOI: 10.1016/j.ast.2015.11.028.

[36] T. Burton, N. Jenkins, D. Sharpe, and E. Bossanyi. *Wind Energy Handbook*. Wiley, 2011. DOI: 10.1002/9781119992714.

[37] J. G. Leishman, M. J. Bhagwat, and A. Bagai. Free-Vortex Filament Methods for the Analysis of Helicopter Rotor Wakes. *Journal of Aircraft*, 39(5):759–775, 2002. DOI: 10.2514/2.3022.

[38] J. Zhang, A. D. Shaw, C. Wang, H. Gu, M. Amoozgar, M. I. Friswell, and B. K. S. Woods. Aeroelastic model and analysis of an active camber morphing wing. *Aerospace Science and Technology*, 111(106534), 2021. DOI: 10.1016/j.ast.2021.106534.

[39] P. B. Ryzhakov, R. Rossi, S. R. Idelsohn, and E. Oñate. A monolithic lagrangian approach for fluid–structure interaction problems. *Computational Mechanics*, 446, 2010. DOI: 10.1007/s00466-010-0522-0.

[40] H. Liu, Y. Qu, H. Gao, F. Xie, and G. Meng. Nonlinear aeroelastic fluid-structure-acoustic interaction analysis of a coupled composite panel with an acoustic cavity in supersonic flow. *Journal of Sound and Vibration*, 569(118086), 2024. DOI: 10.1016/j.jsv.2023.118086.

[41] W. A. Wall, S. Genkinger, and E. Ramm. A strong coupling partitioned approach for fluid–structure interaction with free surfaces. *Computers & Fluids*, 36(1):169–183, 2007. DOI: 10.1016/j.compfluid.2005.08.007.

[42] E. H van Brummelen. Partitioned iterative solution methods for fluid–structure interaction. *International Journal for Numerical Methods in Fluids*, 65(1-3):3–27, 2011. DOI: 10.1002/fld.2465.

[43] J. Degroote, K. L. Bathe, and J. Vierendeels. Performance of a new partitioned procedure versus a monolithic procedure in fluid–structure interaction. *Computers & Structures*, 87(11):793–801, 2009. DOI: 10.1016/j.compstruc.2008.11.013.

[44] T. Richter. A fully Eulerian formulation for fluid–structure-interaction problems. *Journal of Computational Physics*, 233:227–240, 2013. DOI: 10.1016/j.jcp.2012.08.047.

[45] A. Cornejo, A. Franci, F. Zárate, and E. Oñate. A fully Lagrangian formulation for fluid-structure interaction problems with free-surface flows and fracturing solids. *Computers & Structures*, 250(106532), 2021. DOI: 10.1016/j.compstruc.2021.106532.

[46] A. Lozovskiy, M. A. Olshanskii, and Y. V. Vassilevski. Analysis and assessment of a monolithic FSI finite element method. *Computers & Fluids*, 179:277–288, 2019. DOI: 10.1016/j.compfluid.2018.11.004.

[47] S. Tschisgale, B. Löhrer, R. Meller, and J. Fröhlich. Large eddy simulation of the fluid–structure interaction in an abstracted aquatic canopy consisting of flexible blades. *Journal of Fluid Mechanics*, 916(A43), 2021. DOI: 10.1017/jfm.2020.858.

[48] K. Stein, T. Tezduyar, and R. Benney. Mesh moving techniques for fluid-structure interactions with large displacements. *Journal of Applied Mechanics*, 70(1):58–63, 2003. DOI: 10.1115/1.1530635.

[49] K. L. Bathe and H. Zhang. A mesh adaptivity procedure for cfd and fluid-structure interactions. *Computers & Structures*, 87(11):604–617, 2009. DOI: 10.1016/j.compstruc.2009.01.017.

[50] Y. Bazilevs, M. C. Hsu, Y. Zhang, W. Wang, X. Liang, T. Kvamsdal, R. Brekken, and J. G. Isaksen. A fully-coupled fluid-structure interaction simulation of cerebral aneurysms. *Computational Mechanics*, 46:3–16, 2010. DOI: 10.1007/s00466-009-0421-4.

[51] P. Crosetto, P. Reymond, S. Deparis, D. Kontaxakis, N. Stergiopulos, and A. Quarteroni. Fluid–structure interaction simulation of aortic blood flow. *Computers & Fluids*, 43(1):46–57, 2011. DOI: 10.1016/j.compfluid.2010.11.032.

[52] H. Dang, Z. Yang, and Y. Li. Accelerated loosely-coupled CFD/CSD method for nonlinear static aeroelasticity analysis. *Aerospace Science and Technology*, 14(4):250–258, 2010. DOI: 10.1016/j.ast.2010.01.004.

[53] X. Zhao, Y. Zhu, and S. Zhang. Transonic wing flutter predictions by a loosely-coupled method. *Computers & Fluids*, 58:45–62, 2012.

[54] A. O. Mohmmed, H. H. Al-Kayiem, O. Ahmed, and O. Sabir. One-way coupled fluid–structure interaction of gas–liquid slug flow in a horizontal pipe: Experiments and simulations. *Journal of Fluids and Structures*, 97(103083), 2020. DOI: 10.1016/j.jfluidstructs.2020.103083.

[55] K. Wijesooriya, D. Mohotti, A. Amin, and K. Chauhan. Comparison between an uncoupled one-way and two-way fluid structure interaction simulation on a super-tall slender structure. *Engineering Structures*, 229(111636), 2021. DOI: 10.1016/j.engstruct.2020.111636.

[56] E. F. Sheta, V. J. Harrand, D. E. Thompson, and T. W. Strganac. Computational and experimental investigation of limit cycle oscillations of nonlinear aeroelastic systems. *Journal of Aircraft*, 39(1):133–141, 2002. DOI: 10.2514/2.2907.

[57] W. B. Shangguan and Z. H. Lu. Experimental study and simulation of a hydraulic engine mount with fully coupled fluid–structure interaction finite element analysis model. *Computers & Structures*, 82(22):1751–1771, 2004. DOI: 10.1016/j.compstruc.2004.05.017.

[58] G. A. Zarruk, P. A. Brandner, B. W. Pearce, and A.W. Phillips. Experimental study of the steady fluid–structure interaction of flexible hydrofoils. *Journal of Fluids and Structures*, 51:326–343, 2014. DOI: 10.1016/j.jfluidstructs.2014.09.009.

[59] Or Avin, D. E. Raveh, A. Drachinsky, Y. Ben-Shmuel, and M. Tur. Experimental aeroelastic benchmark of a very flexible wing. *AIAA Journal*, 60(3):1745–1768, 2022. DOI: 10.2514/1.J060621.

[60] J. L. Wagner, K. M. Casper, S. J. Beresh, P. S Hunter, R. W. Spillers, J. F. Henfling, and R. L. Mayes. Fluid-structure interactions in compressible cavity flows. *Physics of Fluids*, 27(6), 2015. DOI: 10.1063/1.4922021.

[61] Micro-Epsilon. confocalDT IFS2404 datasheet, 2023.

[62] H. Schlichting. *Boundary Layer Theory*. McGraw-Hill, 7th edition, 1979.

[63] F. Nicoud and F. Ducros. Subgrid-Scale Stress Modelling Based on the Square of the Velocity Gradient Tensor Flow. *Flow Turbulence, and Combustion*, 62(3):183–200, 1999. DOI: 10.1023/A:1009995426001.

[64] J. Bear. *Modeling Phenomena of Flow and Transport in Porous Media*. Springer, 2018.

[65] F. R. Menter. Two-Equation Eddy-Viscosity Turbulence Models for Engineering Applications. *AIAA Journal*, 32(8):1598–1605, 1994. DOI: 10.2514/3.12149.

[66] J. H. Ferzinger, M. Peric, and R. L. Street. *Computational Methods for Fluid Dynamics*. Springer, 4th edition, 2020.

[67] Ansys Inc. *Ansys Fluent Theory Guide, 2023R1*. 2023.

[68] S. Majumdar. Role of underrelaxation in momentum interpolation for calculation of flow with nonstaggered grids. *Numerical Heat Transfer*, 13(1):125–132, 1988. DOI: 10.1080/10407788808913607.

[69] S. F. McCormick. *Multigrid Methods*. SIAM, 1987. DOI: 10.1137/1.9781611971057.

[70] O. C. Zienkiewicz, R. L. Taylor, and J. Z. Zhu. *The Finite Element Method: Its Basis and Fundamentals*. Elsevier, 2005. 10.1016/C2009-0-24909-9.

[71] R. Dorf and R. Bishop. *Modern Control Systems*. Pearson, 13th edition, 2016.

[72] G. A. Papagiannopoulos and G. D. Hatzigeorgiou. On the use of the half-power bandwidth method to estimate damping in building structures. *Soil Dynamics and Earthquake Engineering*, 31(7):1075–1079, 2011. DOI: 10.1016/j.soildyn.2011.02.007.

[73] Ansys Inc. *Ansys Mechanical Theory Guide, 2023R1*. 2023.

[74] J. N. Reddy. *Theory and Analysis of Elastic Plates*. CRC Press, 2006. DOI: 10.1201/9780849384165.

[75] M. A. Hopcroft, W. D. Nix, and T. W. Kenny. What is the Young's Modulus of Silicon? *Journal of Microelectromechanical Systems*, 19(2):229–238, 2010. DOI: 10.1109/JMEMS.2009.2039697.

[76] ASM. *ASM Handbook, Volume 2: Nonferrous Alloys and Special-Purpose Materials*. ASM International, 10th edition, 1991.

[77] M. P. Norton and D. G. Karczub. *Fundamentals of Noise and Vibration Analysis for Engineers*. Cambridge University Press, 2003.

[78] C. Scheffer and P. Girdhar. *Practical Machinery Vibration Analysis & Predictive Maintenance*. Elsevier, 2004. DOI: 10.1016/B978-0-7506-6275-8.X5000-0.

[79] J. Jeong and F. Hussain. On the identification of a vortex. *Journal of Fluid Mechanics*, 285:69–94, 1995. DOI: 10.1017/S0022112095000462.